MIT Libraries | DSpace@MIT

MIT Open Access Articles

Implications and mitigation of model mismatch and covariance contamination for hyperspectral chemical agent detection

The MIT Faculty has made this article openly available. ***Please share*** how this access benefits you. Your story matters.

Citation: Niu, Sidi. "Implications and Mitigation of Model Mismatch and Covariance Contamination for Hyperspectral Chemical Agent Detection." Optical Engineering 52.2 (2013): 026202. © 2013 Society of Photo-Optical Instrumentation Engineers

As Published: http://dx.doi.org/10.1117/1.oe.52.2.026202

Publisher: SPIE

Persistent URL: http://hdl.handle.net/1721.1/78596

Version: Final published version: final published article, as it appeared in a journal, conference proceedings, or other formally published context

Terms of Use: Article is made available in accordance with the publisher's policy and may be subject to US copyright law. Please refer to the publisher's site for terms of use.

Massachusetts Institute of Technology

Optical Engineering

SPIEDigitalLibrary.org/oe

Implications and mitigation of model mismatch and covariance contamination for hyperspectral chemical agent detection

Sidi Niu
Steven E. Golowich
Vinay K. Ingle
Dimitris G. Manolakis

SPIE

Downloaded From: http://opticalengineering.spiedigitallibrary.org/ on 03/28/2013 Terms of Use: http://spiedl.org/terms

Implications and mitigation of model mismatch and covariance contamination for hyperspectral chemical agent detection

Sidi Niu
Northeastern University
360 Huntington Avenue
Boston, Massachusetts 02115
E-mail: niusidi@gmail.com

Steven E. Golowich
MIT Lincoln Laboratory
244 Wood Street
Lexington, Massachusetts 02420

Vinay K. Ingle
Northeastern University
360 Huntington Avenue
Boston, Massachusetts 02115

Dimitris G. Manolakis
MIT Lincoln Laboratory
244 Wood Street
Lexington, Massachusetts 02420

Abstract. Most chemical gas detection algorithms for long-wave infrared hyperspectral images assume a gas with a perfectly known spectral signature. In practice, the chemical signature is either imperfectly measured and/or exhibits spectral variability due to temperature variations and Beers law. The performance of these detection algorithms degrades further as a result of unavoidable contamination of the background covariance by the plume signal. The objective of this work is to explore robust matched filters that take the uncertainty and/or variability of the target signatures into account and mitigate performance loss resulting from different factors. We introduce various techniques that control the selectivity of the matched filter and we evaluate their performance in standoff LWIR hyperspectral chemical gas detection applications. © *2013 Society of Photo-Optical Instrumentation Engineers (SPIE).* [DOI: 10.1117/1.OE.52.2.026202]

Subject terms: hyperspectral imagery; steering vector mismatch; covariance contamination; diagonal loading; robust matched filter.

Paper 121343P received Sep. 18, 2012; revised manuscript received Dec. 18, 2012; accepted for publication Dec. 19, 2012; published online Feb. 4, 2013.

1 Introduction

The remote sensing of gaseous plumes has wide applicability to such diverse areas as chemical warfare agent threat reduction, environmental monitoring, disaster relief, and Earth science. Data adaptive algorithms are generally necessary to suppress the clutter signal while passing that of the plume. Imaging hyperspectral sensors are particularly well-suited to these tasks, as they can simultaneously record spectra from both plume and background regions. The adaptive matched filter (AMF) detector[1] plays a major role in detecting gaseous plumes in hyperspectral imagery.[2,3] If the background statistics are Gaussian, and all inputs to the AMF are known perfectly, then the AMF is known to be optimal under a number of criteria. Even when the non-Gaussian nature of real background data is taken into account, the AMF still is very nearly equal to the optimal linear detector.[4]

In actual use, however, there are a number of challenges to application of the AMF, deriving from imperfect knowledge of the inputs to the detector. There will always be mismatch between the gas signature obtained from a library [see Fig. 1(a)] and that observed, due to the nonlinear relationship between absorption and radiance [see Fig. 1(b)], modulation of the signature by the background and atmosphere, differences in the laboratory and field measurement conditions, and imperfections in the sensor itself. The background mean and covariance statistics are estimates with finite sample support, and the statistics of observed scenes are rarely spatially homogeneous. More significantly, the segmentation into plume and plume-free background pixels is not known *a priori*, so any errors in this process will result in contamination of the background statistics by the plume signature[5–7] (see Fig. 2). All of these effects can combine in complex ways to cause losses in the detection results. The combination of steering vector mismatch and target signal contamination of the plume has been known since the adoption of adaptive processing by the radar community.[8,9] The effect of spatial correlations between the plume and background for hyperspectral gas sensing was noted in Theiler et al.,[10] to which the effect of steering vector mismatch caused by Beer's law was added in Theiler et al.[11]

In order to mitigate the performance degradation resulting from steering vector mismatch and covariance matrix contamination, a robust algorithm employing the diagonal loading technique[12] was developed in the radar community. Performance comparisons among variants of diagonal loading were done by Ward et al.[13] A general loading scheme is executed by Besson[14] et al. who concludes that there is no advantage of using general loading instead of conventional diagonal loading. Although diagonal loading has proved effective for both steering vector mismatch and clutter covariance errors, the selection of diagonal loading level is generally ad-hoc. The robust capon beamformer (RCB) provides an algorithm to compute loading level given knowledge of the uncertainty of the steering vector.[15] However, the estimate of steering vector uncertainty is still not accurate and a conservative strategy is preferred during estimation.

In this paper, we verify the effectiveness of the diagonal loading technique to improve the robustness of the AMF on LWIR hyperspectral chemical gas detection. The rest of the

0091-3286/2013/$25.00 © 2013 SPIE

Downloaded From: http://opticalengineering.spiedigitallibrary.org/ on 03/28/2013 Terms of Use: http://spiedl.org/terms

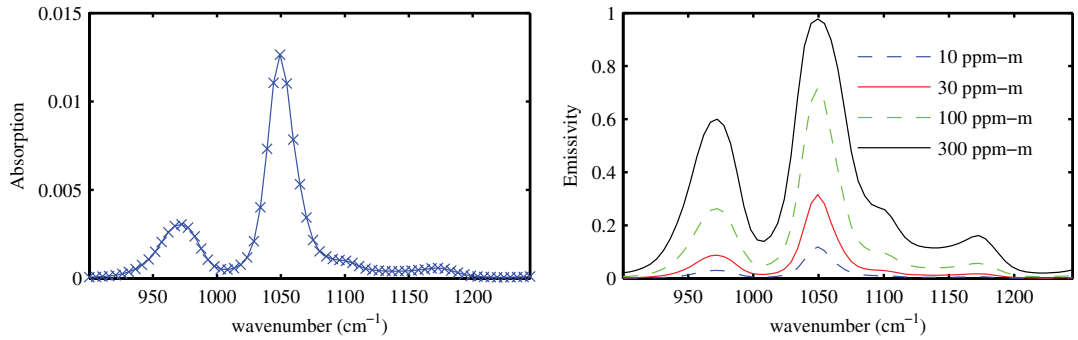

(a) Absorption Spectrum (b) Emissivity

Fig. 1 (a) Library absorbance spectrum for triethyl phosphate (TEP), downsampled to 68 bands and (b) emissivity induced by different concentration path-lengths of gas.

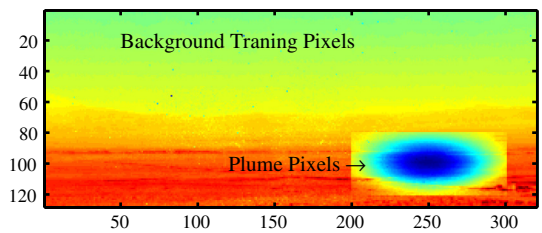

Fig. 2 Mean radiance of the FIRST scene with TEP gas embedded in the southeast corner.

paper is organized as follows. In Sec. 2, the radiance model upon which the study is based is presented. We catalog and verify by experiments the mathematical expressions on performance loss of matched filter due to imperfect estimation in Sec. 3. A robust matched filter based on the diagonal loading technique is studied and realized in Sec. 4 where a variety of experiments are also provided to illustrate the effectiveness of such robust filter. Concluding remarks are given at the end.

2 Radiance Model

The physical basis for gas detection with passive infrared sensors can often be explained with a simplified radiative transfer model,[16] which treats the atmosphere as homogeneous in temperature and transmittance and assumes the chemical plume, if present, to be close to the background. In this model, the at-sensor radiance in the absence of plume, as a function of wavelength, is given by

$$L_{\text{off}}(\lambda) = (1 - \tau_a(\lambda))B(\lambda, T_a) + \tau_a(\lambda)L_b(\lambda), \tag{1}$$

where the two terms on the right side of Eq. (1) represent atmospheric radiance and background radiance modulated by the atmosphere, correspondingly. In Eq. (1), $\tau_a(\lambda)$ is defined to be the atmospheric transmittance, T_a is the temperature of the atmosphere, $L_b(\lambda)$ is the background radiance, and $B(\lambda, T)$ is the Planck function evaluated at wavelength λ and temperature T.

The presence of a plume has two effects: it absorbs part of the background radiation passing through it, and it emits its own radiation. The resulting radiance is subsequently attenuated by transmission through the atmosphere, and is given by

$$L_{\text{on}}(\lambda) = [1 - \tau_a(\lambda)]B(\lambda, T_a) + \tau_a(\lambda)\tau_p(\lambda)L_b(\lambda) + \tau_a(\lambda)[1 - \tau_p(\lambda)]B(\lambda, T_p), \tag{2}$$

where $\tau_p(\lambda)$ is the plume transmittance and T_p its temperature. In Eq. (2), the three terms represent the at-sensor radiance due to the atmosphere, the background radiance as modulated by the plume and atmosphere, and the plume radiance as modulated by the atmosphere.

By substituting $L_{\text{off}}(\lambda)$ into Eq. (2) and with a few simple manipulations, an equivalent radiance expression is obtained

$$L_{\text{on}}(\lambda) = L_{\text{off}}(\lambda) + \tau_a(\lambda)[1 - \tau_p(\lambda)][B(\lambda, T_p) - L_b(\lambda)]. \tag{3}$$

This form is the starting point for most detection algorithms. It expresses the effect of a plume as a contrast between the on- and off-plume radiance. Also, it highlights the importance of the thermal contrast between the plume and the background.

The spectral transmission function, $\tau_p(\lambda)$, of a plume with M gas species can be modeled using Beer's law

$$\tau_p(\lambda) = \exp\left[-\sum_{m=1}^{M} \gamma_m \alpha_m(\lambda)\right]. \tag{4}$$

The function $\alpha_m(\lambda)$, the absorption coefficient spectrum, is unique for each gaseous chemical and can be used as a spectral signature. The quantity γ_m, the concentration path-length (CL), is the integrated concentration of gas along the sensor boresight.

The Eqs. (3) and (4) represent the on-plume radiance as a nonlinear function of the parameters that characterize the plume, atmosphere, and background. However, there are many situations in which simplifying assumptions are both valid and advantageous in terms of algorithmic complexity and intuition. In this paper, we will employ the optically thin plume approximation in which Beer's law may be linearized as

$$1 - \tau_p(\lambda) \approx \sum_{m=1}^{M} \gamma_m \alpha_m(\lambda). \tag{5}$$

Downloaded From: http://opticalengineering.spiedigitallibrary.org/ on 03/28/2013 Terms of Use: http://spiedl.org/terms

Then the signal model Eq. (3) becomes

$$L_{\text{on}}(\lambda) = L_{\text{off}}(\lambda) + \sum_{m=1}^{M} \gamma_m \beta_m(\lambda), \tag{6}$$

with the definition of

$$\beta_m(\lambda) = \tau_a(\lambda)[B(\lambda, T_p) - L_b(\lambda)]\alpha_m(\lambda), \tag{7}$$

as the "in-scene target signature" for optically thin plumes. This model Eq. (6) is linear in the gas concentration path-length γ_m.

The measured radiance depends on the characteristics of the sensor, which we model by convolution with the spectral impulse response function $g(\lambda)$ and the addition of Gaussian noise. If the sensor measures the radiance at K spectral channels centered at wavelength $\lambda_k, k = 1, 2, \ldots, K$, we can organize the measurements in vector form as follows

$$\boldsymbol{x} = \sum_{m=1}^{M} a_m \boldsymbol{s}_m + v, \tag{8}$$

where $\boldsymbol{x}$ is the measured radiance, the a_m are the gas mean concentration-path length products, $\boldsymbol{v}$ is the background plus noise radiance, and $\boldsymbol{s}_m$ is the signature associated with gas m. These are given by

$$a_m = \gamma_m, \tag{9a}$$

$$v_k = (L_{\text{off}} * g)(\lambda)|_{\lambda=\lambda_k} + n_k, \tag{9b}$$

$$s_k^{(m)} = (\beta_m * g)(\lambda)|_{\lambda=\lambda_k}, \tag{9c}$$

where n_k is the noise in channel k. We shall use the terms spectral signature, amount, and background for the quantities $\boldsymbol{s}_m$, a_m, and $\boldsymbol{v}$, respectively.

According to Eqs. (7) and (9c), the steering vector depends on the gas signature, background radiance, atmospheric transmittance, plume temperature, and sensor response. Incomplete knowledge from any of these sources will result in a mismatch of steering vector between the detector and measurement. Within the thin-plume limit, the steering vector in the AMF is linear in the gas signature, which is known from lab measurements. These signatures may not match the observed signal for a variety of reasons, such as calibration or temperature differences, or variations in chemical composition. Thicker plumes will incur even more steering vector mismatch, as the nonlinearity of Beer's law will change the signature. When the background cannot be approximated as flat, the plume contrast signal will be affected by the background emissivity if it has spectral structure that overlaps that of the gas signature. In this case, the observed plume signature will depend on the background radiance. The atmospheric transmittance also appears in the steering vector. It generally is known only roughly from environmental data and must be estimated from the observed spectra over the scene. Estimation errors in this quantity will propagate through to the detector. Hence, some amount of steering vector mismatch is inevitable.

3 SCR Loss Study

The signal-to-clutter ratio (SCR) is a natural performance measure for the AMF. As a single summary statistic, it does not capture all of the details of detection performance, but we argue in Sec. 4.3 that it can provide a reliable guide for some scenarios. Furthermore, its mathematical simplicity can provide valuable intuition. In this section, we will catalog mathematical expressions for the SCR loss in a number of different situations. These expressions are then verified by idealized experiments and also compared to more realistic experiments that incorporate more of the variability that is seen in measured data.

3.1 *Theoretical SCR Loss Expressions*

We first rephrase the theoretical SCR loss expressions resulting from various situations of knowledge imperfection which is well treated in radar community.

3.1.1 *Signal-to-clutter ratio*

Our signal model throughout this section is that of Eq. (8) with a single gas

$$\boldsymbol{x} = a\boldsymbol{s}_0 + \boldsymbol{v}, \tag{10}$$

where $\boldsymbol{x}$ is the observed radiance, $\boldsymbol{v}$ is the background radiance plus noise, and $\boldsymbol{s}_0$ is the actual steering vector, or plume signature. The matched filter detector is defined to be

$$\text{MF}(z; s, \Sigma, \boldsymbol{\mu}) = \boldsymbol{s}^T \Sigma^{-1}(z - \boldsymbol{\mu}), \tag{11}$$

where z is an observed radiance, $\boldsymbol{s}$ is the assumed steering vector, Σ is a covariance matrix, and $\boldsymbol{\mu}$ is the assumed mean background radiance. The definition of the SCR is the squared ratio of the output of the matched filter applied to $\boldsymbol{\mu} + a\boldsymbol{s}_0$ and the standard deviation of the matched filter applied to pure background $\boldsymbol{v}$

$$\text{SCR} = \frac{\text{MF}(\boldsymbol{\mu} + a\boldsymbol{s}_0; \boldsymbol{s}, \Sigma, \boldsymbol{\mu})^2}{\langle \text{MF}(\boldsymbol{v}; \boldsymbol{s}, \Sigma, \boldsymbol{\mu})^2 \rangle} = \frac{a^2(\boldsymbol{s}^T\Sigma^{-1}\boldsymbol{s}_0)^2}{\boldsymbol{s}^T\Sigma^{-1}\Sigma_v\Sigma^{-1}\boldsymbol{s}}. \tag{12}$$

We will now evaluate Eq. (12) for a number of cases. The results are most conveniently written in terms of the Mahalanobis trigonometric functions

$$\cos^2_\Sigma(\boldsymbol{x}, \boldsymbol{y}) = \frac{(\boldsymbol{x}^T\Sigma^{-1}\boldsymbol{y})^2}{(\boldsymbol{x}^T\Sigma^{-1}\boldsymbol{x})(\boldsymbol{y}^T\Sigma^{-1}\boldsymbol{y})}, \tag{13a}$$

$$\sin^2_\Sigma(\boldsymbol{x}, \boldsymbol{y}) = 1 - \cos^2_\Sigma(\boldsymbol{x}, \boldsymbol{y}). \tag{13b}$$

We also define the corruption of the covariance matrix by the plume signal as

$$\Sigma_x = \langle (\boldsymbol{x} - \bar{\boldsymbol{x}})(\boldsymbol{x} - \bar{\boldsymbol{x}})^T \rangle = \Sigma_v + \sigma_a^2 \boldsymbol{s}_0 \boldsymbol{s}_0^T + \sigma_a \zeta \boldsymbol{s}_0^T + \sigma_a \boldsymbol{s}_0 \zeta^T, \tag{14}$$

where the operation $\langle \cdot \rangle$ computes the spatial mean value across all pixels, and the plume amplitude variation σ_a^2 and correlation between plume amplitude and background ζ are, respectively,

Downloaded From: http://opticalengineering.spiedigitallibrary.org/ on 03/28/2013 Terms of Use: http://spiedl.org/terms

$$\sigma_a^2 = \langle (a - \bar{a})^2 \rangle, \tag{15}$$

and

$$\zeta = \left\langle \frac{(a - \bar{a})}{\sigma_a} (\boldsymbol{v} - \bar{\boldsymbol{v}}) \right\rangle. \tag{16}$$

Next we summarize the SCR loss expressions for different situations. We note that, throughout the paper, the contamination of the background radiance covariance matrix by the plume signal will be considered, but not contamination of the mean vector. We do not consider the latter because our primary concern is in effects that fundamentally influence the separability of the plume from the background, while corruption of the mean vector causes only a uniform shift in the scores generated by the linear AMF. Such a shift is consequential in the context of a full detection signal processing chain, but this larger issue will be considered elsewhere.

3.1.2 *Optimal case*

First is the optimal case when there is no signature mismatch and perfect background estimation. By plugging the $\boldsymbol{s} = \boldsymbol{s}_0$ and $\Sigma = \Sigma_v$ into Eq. (12), we may use a result of Reed[9] to derive the expression of theoretically best performance as a quadratic function of gas strength

$$\mathrm{SCR} = a^2 \boldsymbol{s}_0^T \Sigma_v^{-1} \boldsymbol{s}_0. \tag{17}$$

3.1.3 *Signature mismatch*

When the steering vector $\boldsymbol{s}$ used in the matched filter does not match that of the plume $\boldsymbol{s}_0$, while the covariance estimate remains perfect, $\Sigma = \Sigma_v$, a loss is incurred that depends on the amount of mismatch. The mismatch loss expression is given by Cox[8] as

$$\mathrm{SCR}_b = \mathrm{SCR}_o \cos^2_{\Sigma_v}(\boldsymbol{s}, \boldsymbol{s}_0). \tag{18}$$

3.1.4 *Covariance corruption*

The next case we consider is that of no steering vector mismatch, $\boldsymbol{s} = \boldsymbol{s}_0$, but with the covariance matrix corrupted by the plume signal,

$$\Sigma = \Sigma_v + \sigma_a^2 \boldsymbol{s}_0 \boldsymbol{s}_0^T + \sigma_a \zeta \boldsymbol{s}_0^T + \sigma_a \boldsymbol{s}_0 \zeta^T. \tag{19}$$

The resulting SCR loss is given by

$$\mathrm{SCR}_c = \frac{\mathrm{SCR}_o}{1 + \frac{\sigma_a^2}{a^2} \mathrm{SCR}_o (\zeta^T \Sigma_v^{-1} \zeta) \sin^2_{\Sigma_v}(\boldsymbol{s}_0, \zeta)}. \tag{20}$$

This expression is also addressed by Theiler in a slightly different form.[11] We observe a saturation effect in Eq. (22) for large values of SCR. If the values of σ_a^2/a^2 and ζ remain constant, then the value of SCR_c approaches an asymptote with increasing SCR.

3.1.5 *Signature mismatch and covariance corruption*

Next we allow both steering vector mismatch and covariance contamination by the plume; however, we first consider the case of no plume-background correlation, so $\zeta = 0$ and

$$\Sigma = \Sigma_v + \sigma_a^2 \boldsymbol{s}_0 \boldsymbol{s}_0^T. \tag{21}$$

The expression for SCR in this case is still analytically tractable, with the result[8]

$$\mathrm{SCR}_d = \frac{\mathrm{SCR}_o \cos^2_{\Sigma_v}(\boldsymbol{s}, \boldsymbol{s}_0)}{1 + \left(2 + \frac{\sigma_a^2}{a^2} \mathrm{SCR}_o\right) \left(\frac{\sigma_a^2}{a^2} \mathrm{SCR}_o\right) \sin^2_{\Sigma_v}(\boldsymbol{s}, \boldsymbol{s}_0)}. \tag{22}$$

Since the numerator of Eq. (22) is first order in SCR_o while the denominator is second order, SCR_d first increases to a peak and then decreases as SCR_o increases.

When the steering vector mismatch vanishes in Eq. (24), the well known result[11] is that the SCR attains its optimal value. In other words, contamination by the plume vector does not incur loss when the steering vector is known exactly, as long as there is no plume-background correlation.

3.1.6 *Most general case*

When the restriction of zero correlation vector ζ is relaxed, when both steering vector mismatch and covariance contamination by the plume are present, a succinct expression for SCR loss is no longer available. However, this is the case most often obtained in practice, so numerical results will be presented in the following experiments.

3.2 *Experimental Validation Setup*

Our experiments are based on simulated plumes algorithmically embedded in a measured background image. This approach allows us to avoid the problem of limited and inexact ground truth resulting from the observations of real plumes and also allows us vastly more flexibility in the placement and properties of the plumes. Figure 3 shows the mean image of the background scene which is a 128×320 first data[16,17] cube with 68 usable spectral bands. The absorption spectrum of the gas spetcies employed in embedding, triethyl phosphate (TEP),[18] is illustrated in Fig. 1(a).

A variety of plume shapes will be employed to probe various effects, as discussed below. These plume profiles are shown in Figs. 4 and 5. Those in Fig. 4 are of constant amplitude, with all pixels under the mask embedded with the same amount of gas. We will use the constant mask to verify our derivation of SCR expressions derived in the precious section. As shown in Fig. 4, three different mask profiles are employed. The first one is a fixed size, horizontally oriented, rectangular mask covering land pixels. The second is similar to the first, but the horizontal size is allowed to vary. The third is again of fixed size, but the orientation is allowed to rotate, which allows the mask to sweep over different background materials. These three profiles are used in

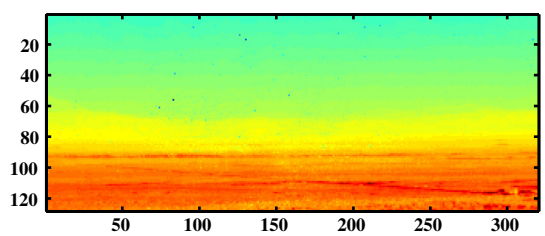

Fig. 3 Mean radiance of the FIRST scene.

Downloaded From: http://opticalengineering.spiedigitallibrary.org/ on 03/28/2013 Terms of Use: http://spiedl.org/terms

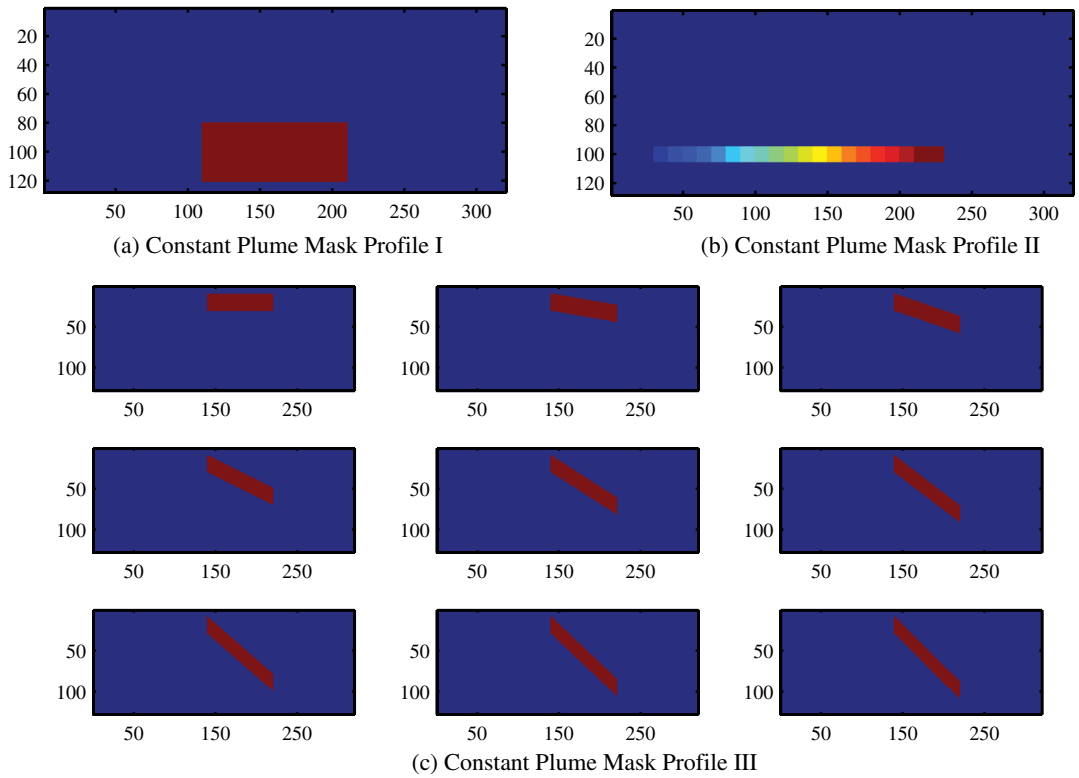

Fig. 4 Constant-amplitude plume mask profiles: (a) fixed size horizontally oriented rectangular mask deployed over lower (land) region of image; (b) variable sized horizontally oriented rectangular mask, again covering land pixels and; (c) fixed size rotating mask that sweeps over different background materials. The correlation between plume and background is smalled for vertical orientations.

different experiments to enable us to analysis the performance degradation due to various factors. Figure 5 consists of three Gaussian distributed amplitude counterparts to Fig. 4. These masks with the highest amounts of gas in the center are used to model a more realistic situation.

Once the desired plume profile is fixed, two methods are employed to embed a simulated plume over the background image: an approximate, linearized technique, and a more accurate, nonlinear method. Since the former is based on the latter, we will describe the latter first. We begin with the assumption that the plume is in thermal equilibrium with the atmosphere. This assumption leads to a simplification of the on-plume radiance Eq. (2), resulting in the form

$$L_{\text{on}}(\lambda) = L_{\text{off}}(\lambda)\tau_p(\lambda) + [1 - \tau_p(\lambda)]B(\lambda, T_a). \tag{23}$$

We observe that the on-plume radiance can be obtained from the off-plume radiance with only knowledge of the atmospheric temperature T_a and the plume transmittance τ_p. In particular, the atmospheric transmittance is not required, though its influence is still present in L_{off}. The value of T_a may be estimated from bands in which the atmosphere is largely opaque due to water vapor, and that of τ_p from Beer's law Eq. (4) with knowledge of the absorbance spectrum $\alpha(\lambda)$ and the mean concentration-path length product γ.

An idealized linear plume embedding is also helpful for comparison, in order to assess the impact of the nonlinear behavior on the results. For this type of embedding, we begin by the full embedding of Eq. (25) over a plume mask with a constant value of the concentration-path length γ. The background variation due to the nonlinearities is removed by taking a spatial mean, and a steering vector is formed with normalizing by γ, with the result

$$s_0 = \frac{1}{\gamma}\langle L_{\text{on}} - L_{\text{off}}\rangle. \tag{24}$$

The resulting approximate radiance expression is

$$L_{\text{on}} \simeq L_{\text{off}} + \gamma s_0, \tag{25}$$

which is exactly of the form Eq. (10). In the limit of small γ and with a spatially constant background radiance L_b, the exact radiance Eq. (3) reduces to the linear form Eq. (25), which justifies the latter. We note that referring to this embedding method as "linear" is a misnomer for larger values of CL, as s_0 has a dependence on CL in the nonlinear Beer's law regime. However, the justification for the term is that nonlinear dependence on the *background* has been removed, as exactly the same signal vectors are present in every pixel of the plume.

3.3 *Experimental Validation Results*

In this section, we provide our experiment results and explanations. There are in total four sets of three experiments each, with each set comprised of constant mask linear embedding, constant mask nonlinear embedding, and Gaussian mask nonlinear embedding. Throughout all the experiments, since the steering vector is pixel dependent except the ideal linear embedding, we use the mean vector of all pixel-wise steering vectors as the true one we feed to

Downloaded From: http://opticalengineering.spiedigitallibrary.org/ on 03/28/2013 Terms of Use: http://spiedl.org/terms

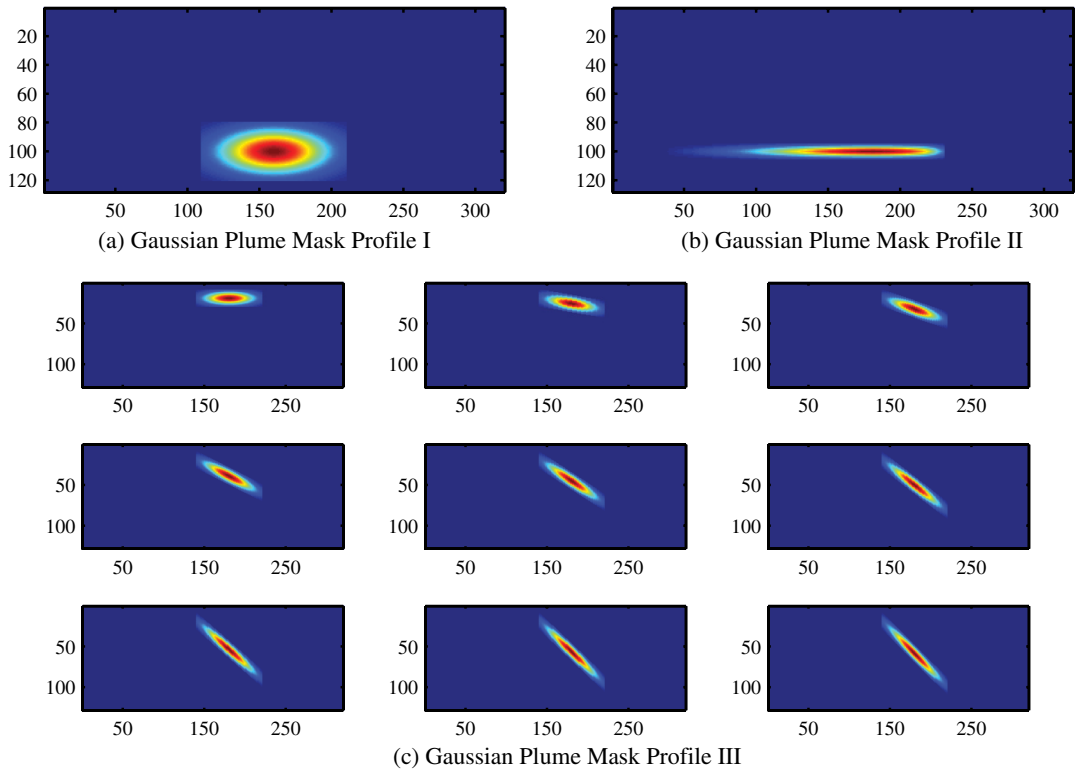

Fig. 5 Gaussian distributed amplitude plume mask profiles. The plume amplitude is highest in the center and monotonically decreases away from the center. The fixed and variable size and orientation masks (a) though (c) are otherwise as in Fig. 4.

our optimal matched filter. This setup will bring obvious deviation between theoretical and experimental results when the variance within pixel-wise steering vectors is large, as a Gaussian profile mask embedding applies.

The purpose of the first set of experiments is to study the performance loss due to steering vector mismatch alone discussed in Sec. 3.1.3. We use the masks in Figs. 4(a) and 5(a). The mismatch is introduced by rotating the true steering vector $\boldsymbol{s}_0$ along an arbitrary, randomly chosen direction by amounts that result in Mahalanobis cosine values in the set $\cos^2_\Sigma(\boldsymbol{s},\boldsymbol{s}_0) = 0.2, 0.3, \ldots, 1$. The gas CL across the constant mask is 10 ppm-m and that of the Gaussian mask is set so its mean is 10 ppm-m. Figure 6 shows the SCR loss plots. As shown in Fig. 6(a), with the signature mismatch increasing, the SCR loss is exactly the product of the optimal SCR and Mahalanobis cosine squared; the experimental plot overlaps the theoretical one nearly everywhere, verifying the SCR expressions of Eqs. (17) and (18). In Fig. 6(b), the empirical plot also fits the theoretical one quite well because there is very little variation in the pixel radiances included in the embedding mask. In Fig. 6(c), there is an explicit deviation between the theoretical (using the mean steering vector) and empirical plots because the gas amplitude is Gaussian distributed, which results in pixel dependent steering vectors due to Beer's law. For all three plots, we can see that the performance degrades strictly linearly with respect to the signature mismatch. Because of this dependence, the deviation between the estimated and true steering vector must be quite large in order to cause a large SCR loss.

The second experiment involves the combination of two effects, steering vector mismatch and covariance contamination by the plume discussed in Sec. 3.1.5. However, the plume-background correlation ζ, defined in Eq. (16), is taken to be identically zero, the case that is covered by the analytic expression in Eq. (22). Although this expression covers an idealized limiting case, the results are instructive as to the importance of the correlation parameter. The dependence on ζ will be further explored below.

We guarantee zero correlation by duplicating the image and embedding gas in one half of the resulting image, a method due to Theiler.[11] After gas releasing imagery scene and embedding mask are shown in Fig. 7(a) and 7(b), respectively. This setup pairs each pixel with another with identical background radiance and magnitude gas strength deviation from the mean, but of different sign. Hence, the terms in Eq. (16) pairwise sum to zero and correspondingly result in zero correlation. We next compute SCR as a function of CL. The gas amplitude is varied from 1 ppm-m to 10 ppm-m, which includes both the linear and nonlinear regimes. When using the linear embedding method, we always use the exact value of the steering vector given by Eq. (25), even as it is modulated by Beer's law, despite the fact that knowledge of the plume strength is difficult to obtain in practice. This choice is made because our interest is in finding fundamental limits of SCR.

In Fig. 8(a), the SCR of the case of covariance corruption with mismatch is shown to overplot the theoretical one, verifying Eq. (22). Furthermore, it coincides with the optimal SCR performance, verifying the prediction that the inclusion of a rank one perturbation from the plume signal does not affect detection, if there is no steering vector mismatch. The deviation of the experimental curve from that predicted by theory in Fig. 8(b) is due to the variations in the true steering vector induced by Beer's law. Another insight from this

Downloaded From: http://opticalengineering.spiedigitallibrary.org/ on 03/28/2013 Terms of Use: http://spiedl.org/terms

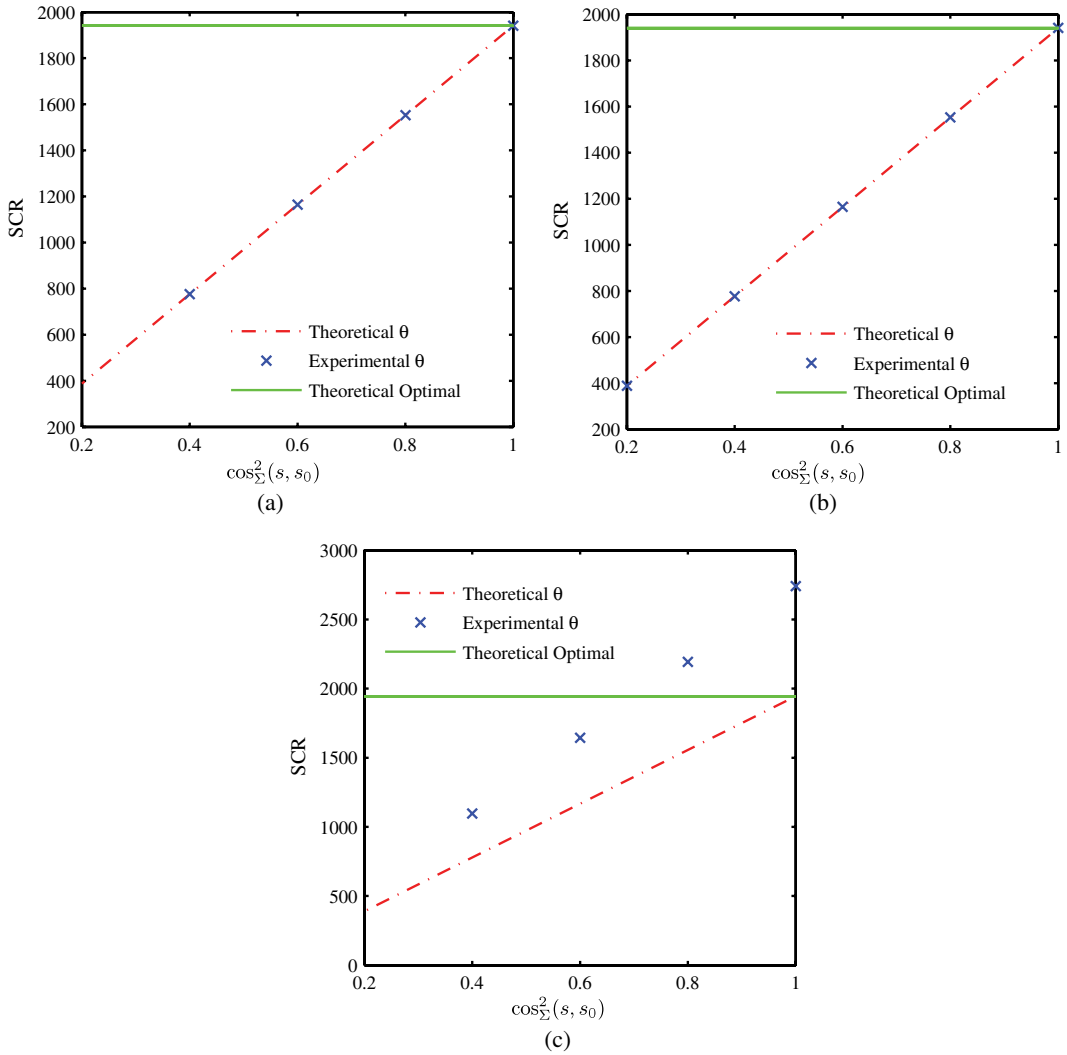

Fig. 6 SCR loss study due to steering vector mismatch alone, with the gas CL set to $a = 10$ ppm-m. The performance loss is linear with respect to the Mahalanobis cosine squared in Eq. (18). Abbreviation "θ" implies mismatch in steering vector. (a) Constant mask linear embedding case with the empirical plot (blue dash line with × marker) overlapping theoretical one (red dash line) perfectly; (b) constant mask nonlinear embedding and; (c) Gaussian mask nonlinear embedding.

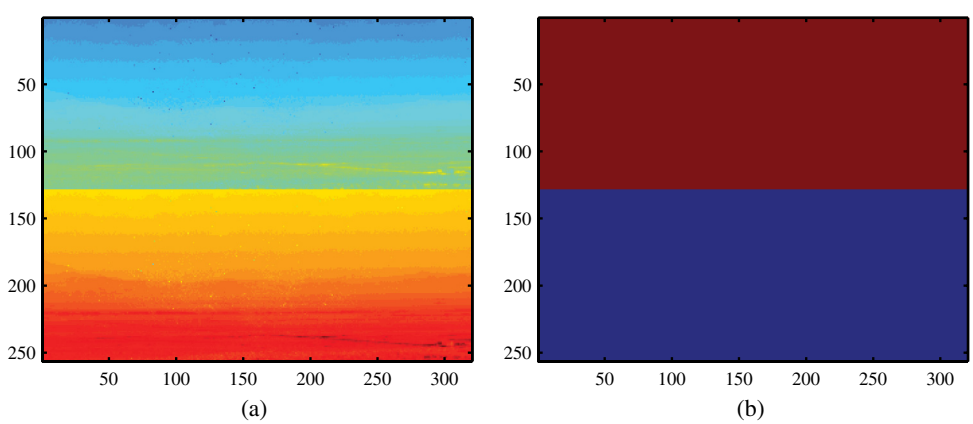

Fig. 7 (a) Matched image pair embedded plume mask and; (b) matched image embedding mask.

Downloaded From: http://opticalengineering.spiedigitallibrary.org/ on 03/28/2013 Terms of Use: http://spiedl.org/terms

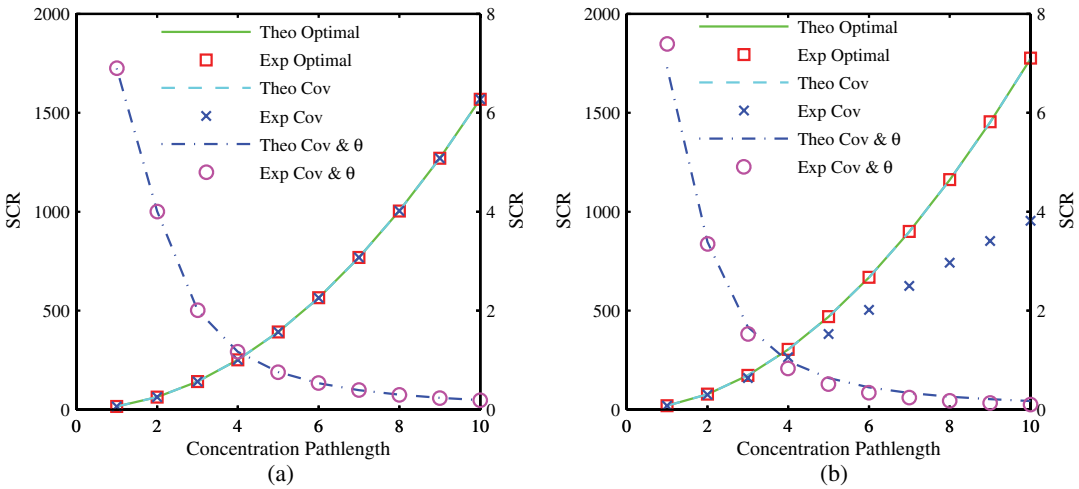

Fig. 8 SCR loss study when the plume background correlation vector ζ equals zero. Left y-axis corresponds to optimal cases when SCR is extremely large and right y-axis is metric for lower SCR when mismatch and contamination happen. Abbreviation "θ" implies mismatch in steering vector while "Cov" means the detector suffers from covariance corruption. (a) Linear embedding and (b) nonlinear embedding.

experiment we want to emphasize is that, because it is constructed so that $\zeta = 0$, it corresponds to the only case that a tractable analytical expression is available for both corruption and mismatch.

The third set of experiments again explores the variation of SCR with CL, but this time with a non-zero plume-background correlation, discussed in Sec. 3.1.4, due to the masks in Figs. 4(a) and 5(a). When the concentration path-length a increases, the standard deviation σ_a also increases, but the ratio σ_a^2/a^2 remains constant. The optimal SCR under ideal conditions Eq. (17) is predicted to increase quadratically with CL, but when the covariance is corrupted by the plume signal and plume-background correlation is present, the increase saturates to an asymptotic value, though it is still monotonic Eq. (20). The effect is accentuated by the large value of the Mahalanobis sine term in Eq. (20), which is close to unity. We will see below that this term is generally expected to be large. The optimal and saturated behaviors are demonstrated in Fig. 9, both for the linear embedding (a), as well as the nonlinear case with constant CL profile (b) and Gaussian (c). In all cases a close agreement with theory is seen, with small deviations in (c) due to the steering vector variation due to Beer's law. The performance degradation due the combination of covariance corruption and plume-background correlation, even with a perfect steering vector match, is dramatic. The inclusion of even a small amount of steering vector mismatch causes even further SCR loss discussed in Sec. 3.1.6. This last case is demonstrated in Fig. 9 with a mismatch value of $\cos^2_\Sigma(\boldsymbol{s}, \boldsymbol{s}_0) = 0.95$. For the purpose of clear illustration, two scales are employed in each subplot where left y-axis corresponds to optimal performance (red and blue lines) while right y-axis corresponds to degraded performance (green, magenta, and cyan lines).

The fourth set of experiments probes the effects of varying the plume size, using the set of embedding masks from Figs. 4(b) and 5(b), discussed in Secs. 3.1.4 and 3.1.6. The gas CL is held constant as 2 ppm-m, so increasing the plume size results in σ_a increasing monotonically, while $\|\zeta\|$ may either increase or decrease depending on the details of the background. The theory Eq. (22) for the case of covariance corruption without steering vector mismatch predicts that SCR will decrease with increasing σ_a and increasing $\|\zeta\|$, which is borne out by the results in Fig. 10. A small steering vector mismatch is also introduced, with $\cos^2_\Sigma(\boldsymbol{s}, \boldsymbol{s}_0) = 0.95$. The difference between the theoretical and empirical plots in Fig. 10(c) is, as before, due to the Beer's law, variation along with the spatial variation of the background pixels under the plume.

The final set of experiments, also to verify conclusions in Secs. 3.1.4 and 3.1.6, quantify the effects of varying plume-background correlation, with the plume spatial variance σ_a held constant at $\sigma_a = 0.9976$ ppm-m during the rotation of constant mask and $\sigma_a = 1.2625$ ppm-m during the rotation of Gaussian mask. These conditions are achieved by the use of the masks in Figs. 4(c) and 5(c). Because of the structure of background scene used, the plume-background correlation $\|\zeta\|$ is large when a horizontal rectangular mask is employed. This correlation vector decreases in magnitude when the mask is oriented vertically. During the rotation of the mask, the number of pixels in the mask remains the same, so and σ_a remains constant. However, as shown in Fig. 11, $\zeta^T\Sigma_v^{-1}\zeta$ decreases and the performance goes up. The Mahalanobis trigonometric $\sin^2_{\Sigma_v}(s_0, \zeta)$ almost equal to 1 during all experiments due to the large dimensionality and its contribution to the overall SCR is minor. As with the previous experiments, the case of steering vector mismatch is included, with a mismatch of $\cos^2_\Sigma(\boldsymbol{s}, \boldsymbol{s}_0) = 0.95$.

4 Robust Matched Filter

In this section, we will describe the design of a robust matched filter employing the diagonal loading technique[12] to mitigate the performance loss seen in the previous section and verify the resulting performance improvement through experiments.

4.1 *Robust Matched Filter Derivation*

We recall our signal model with a single gas, first defined in Eq. (10):

$$\boldsymbol{x} = a\boldsymbol{s}_0 + \boldsymbol{v}.$$

Downloaded From: http://opticalengineering.spiedigitallibrary.org/ on 03/28/2013 Terms of Use: http://spiedl.org/terms

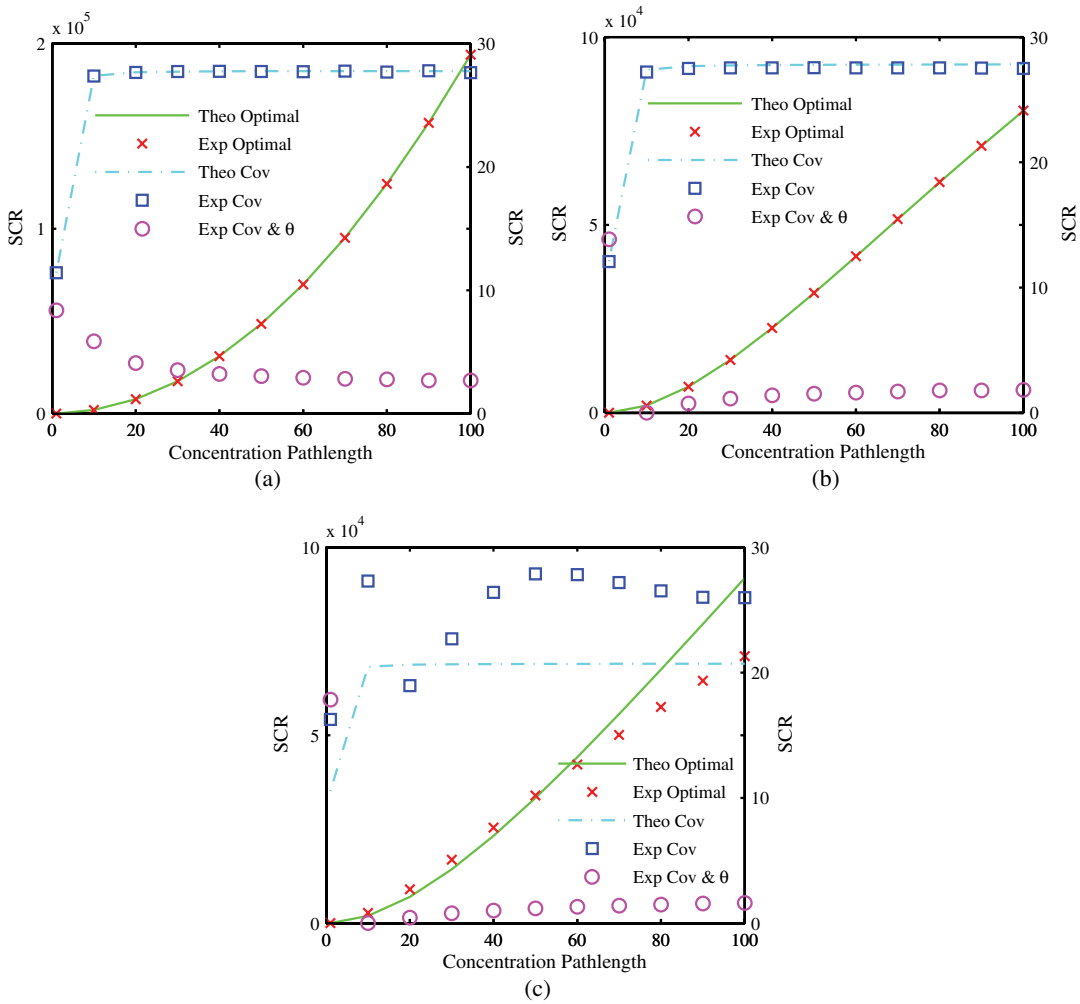

Fig. 9 SCR loss due to covariance contamination and plume-background correlation, with and without steering vector mismatch, as a function of gas concentration path-length. Abbreviation "θ" implies mismatch in steering vector while "Cov" means the detector suffers from covariance corruption. (a) Constant mask linear embedding; (b) constant mask nonlinear embedding and; (c) Gaussian mask nonlinear embedding.

A linear filter detector is defined as

$$y = \boldsymbol{h}^T \boldsymbol{x}. \tag{26}$$

The optimal matched filter is defined to maximize the SCR, defined in Eq. (12), which can be rewritten as

$$\mathrm{SCR} = \frac{\mathrm{SignalPower}}{\mathrm{ClutterPower}} = \frac{a^2(\boldsymbol{h}^T \boldsymbol{s}_0)^2}{\boldsymbol{h}^T \Sigma_v \boldsymbol{h}}. \tag{27}$$

Since the above definition is a ratio and its value is invariant to scaling of $\boldsymbol{h}$, another constraint is applied to the norm of $\boldsymbol{h}$ in order to guarantee the uniqueness of optimal $\boldsymbol{h}$,

$$\boldsymbol{h}^T \boldsymbol{s}_0 = 1. \tag{28}$$

Hence the maximization of the ratio SCR is equivalent to minimization of its denominator $\boldsymbol{h}^T \Sigma_v \boldsymbol{h}$ with constraint in Eq. (28), and the resulting optimal matched filter is

$$\boldsymbol{h}_{\mathrm{opt}} = \frac{\Sigma_v^{-1} s_0}{\boldsymbol{s}_0^T \Sigma_v^{-1} \boldsymbol{s}_0}. \tag{29}$$

As explained in the previous section, in real world applications, our knowledge of the steering vector is always imperfect which results in deviation between the supposed steering vector $\boldsymbol{s}$ and the true one $\boldsymbol{s}_0$. Additionally, the estimate of background covariance Σ converges to Σ_v theoretically only with the availability of an infinite number of plume-free background samples. In practice, only a limited number of samples are available, with many of them corrupted because of the presence of the plume.

In order to overcome the sensitivity to steering vector mismatch and covariance contamination of the matched filter, the development of a robust algorithm is highly desirable. This problem has been traditionally dealt with using a diagonal loading approach or an eigenspace-based approach.[12] Furthermore, the RCB[15] has been formulated as a diagonal loading problem.

Suppose that we have the knowledge about the steering vector $\boldsymbol{s}$ that it belongs to an uncertainty ellipsoid centered at $\boldsymbol{s}_0$

$$(\boldsymbol{s} - \boldsymbol{s}_0)^T C^{-1} (\boldsymbol{s} - \boldsymbol{s}_0) \leq 1, \tag{30}$$

where C is a positive definite matrix. Since it is difficult to reliably estimate the full matrix C in most cases, we usually set $C = \varepsilon \boldsymbol{I}$, so that Eq. (30) becomes

$$\|\boldsymbol{s} - \boldsymbol{s}_0\|^2 \leq \varepsilon, \tag{31}$$

Downloaded From: http://opticalengineering.spiedigitallibrary.org/ on 03/28/2013 Terms of Use: http://spiedl.org/terms

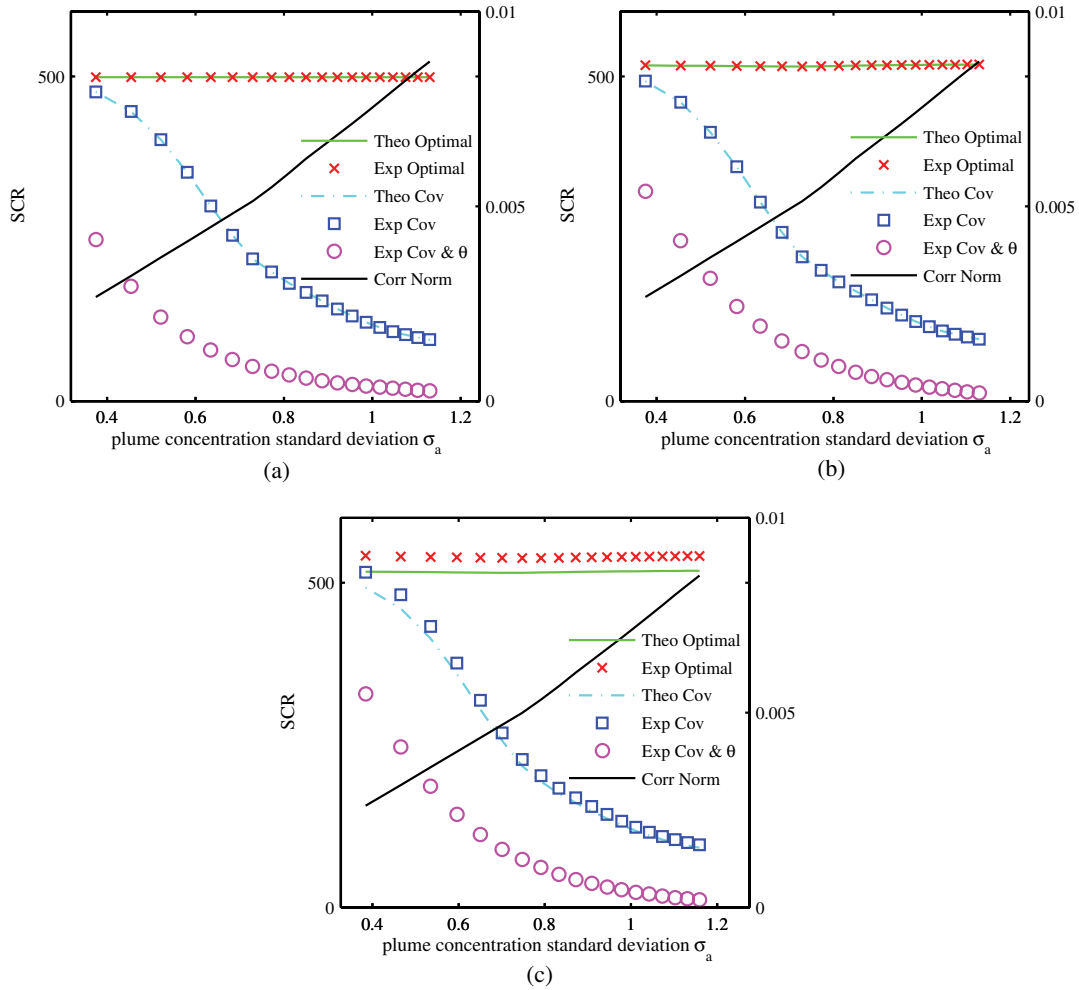

Fig. 10 SCR loss due to covariance contamination and plume-background correlation, with and without steering vector mismatch, as a function of plume size. Right *y*-axis corresponds to the plume-background correlation norm. Abbreviation "θ" implies mismatch in steering vector while "Cov" means the detector suffers from covariance corruption. (a) constant mask linear embedding; (b) Constant mask nonlinear embedding and; (c) Gaussian mask nonlinear embedding.

where ε is a positive number. It has been shown that the robust matched filter (RMF) can be obtained as the solution to the following optimization problem[15]

$$\min_s \boldsymbol{s}^T \Sigma^{-1} \boldsymbol{s} \text{ subject to } \|\boldsymbol{s} - \boldsymbol{s}_0\|^2 \leq \varepsilon. \tag{32}$$

It turns out that the solution of Eq. (32) occurs on the boundary of the constraint set; therefore, we can reformulate Eq. (32) as a quadratic optimization problem with a quadratic equality constraint

$$\min_s \boldsymbol{s}^T \Sigma^{-1} \boldsymbol{s} \text{ subject to } \|\boldsymbol{s} - \boldsymbol{s}_0\|^2 = \varepsilon. \tag{33}$$

This problem can be efficiently solved using the method of Lagrange multipliers. The solution involves an estimated steering vector

$$\hat{\boldsymbol{s}} = \beta(\Sigma^{-1} + \beta \boldsymbol{I})^{-1} \boldsymbol{s}_0, \tag{34}$$

which is subsequently used to determine the RMF by

$$\boldsymbol{h}_\beta = \frac{\Sigma^{-1}\hat{\boldsymbol{s}}}{\hat{\boldsymbol{s}}^T \Sigma^{-1} \hat{\boldsymbol{s}}}. \tag{35}$$

The Lagrange multiplier $\beta \geq 0$ can be obtained by solving the nonlinear equation

$$\boldsymbol{s}_0^T (\boldsymbol{I} + \beta\Sigma)^{-2} \boldsymbol{s}_0 = \sum_{k=1}^{L} \frac{|\tilde{s}_k|^2}{(1 + \beta\lambda_k)^2} = \varepsilon, \tag{36}$$

where λ_k and $\tilde{s}_k$ are obtained from the eigen-decomposition

$$\Sigma = \boldsymbol{Q} \Lambda \boldsymbol{Q}^T = \sum_{k=1}^{L} \lambda_k \boldsymbol{q}_k \boldsymbol{q}_k^T \tag{37}$$

and the orthogonal transformation

$$\tilde{s} = \boldsymbol{Q}^T \boldsymbol{s}. \tag{38}$$

The solution of Eq. (36) can be easily found using a nonlinear optimization algorithm, for example, Newton's method.

Downloaded From: http://opticalengineering.spiedigitallibrary.org/ on 03/28/2013 Terms of Use: http://spiedl.org/terms

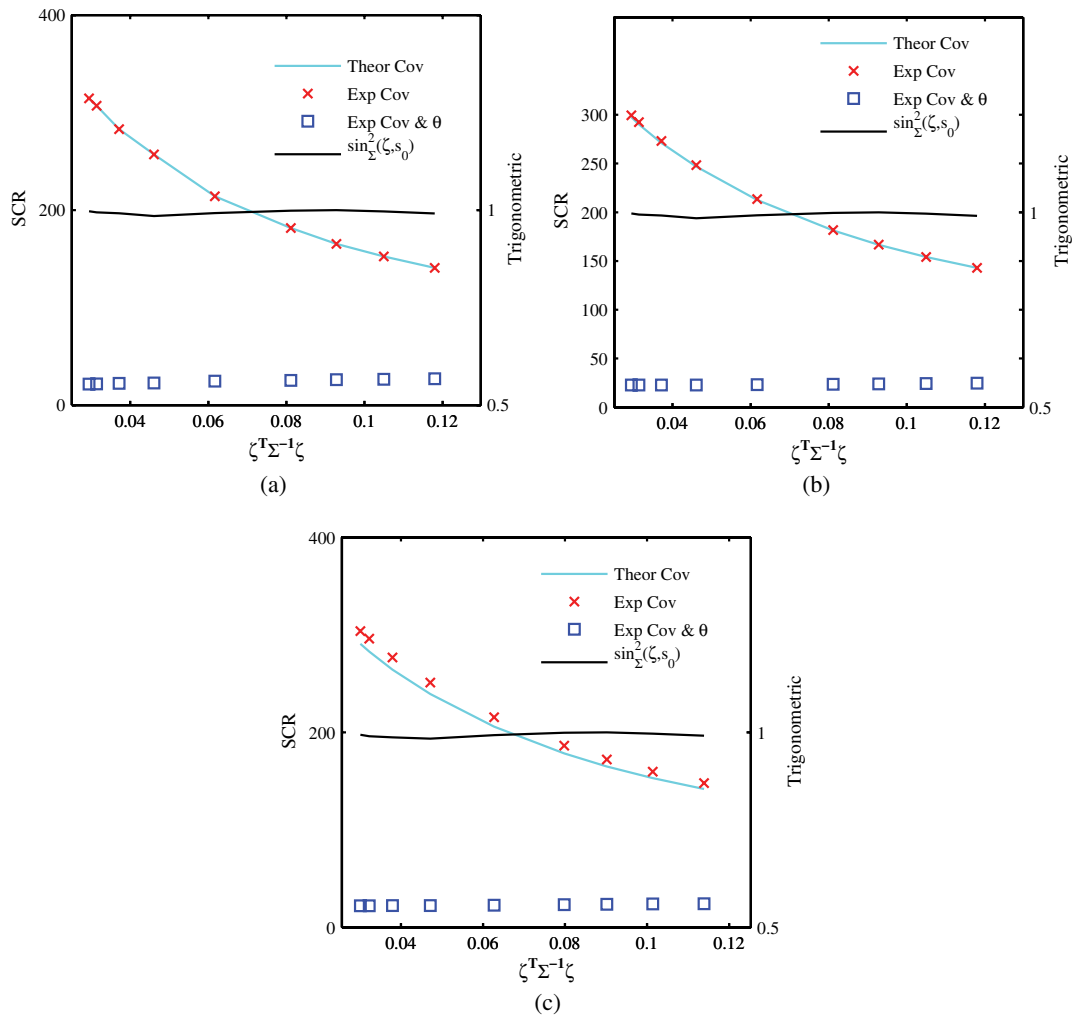

Fig. 11 SCR loss due to covariance contamination and plume-background correlation, with and without steering vector mismatch, as a function of correlation magnitude $\|\zeta\|$. Right y-axis corresponds to the value $\sin^2_\Sigma(\zeta, s_0)$. Abbreviation "$\theta$" implies mismatch in steering vector while "Cov" means the detector suffers from covariance corruption. (a) Constant mask linear embedding; (b) constant mask nonlinear embedding and; (c) Gaussian mask nonlinear embedding.

Finally, the robust matched filter can be expressed in diagonal loading form as follows

$$\boldsymbol{h}_\beta = \frac{(\Sigma + \beta^{-1}\boldsymbol{I})^{-1}\boldsymbol{s}_0}{\boldsymbol{s}_0^T(\Sigma + \beta^{-1}\boldsymbol{I})^{-1}\Sigma(\Sigma + \beta^{-1}\boldsymbol{I})^{-1}\boldsymbol{s}_0}, \tag{39}$$

where β^{-1} is the loading factor computed from Eq. (36).

4.2 *Simulation Experiments Setup*

A variety of experiments were designed to examine the diagonal loading effects on different performance loss factors including steering vector mismatch, contamination level of covariance matrix and fill factor of the plume compared to the whole image. Figure 12(a) shows a Gaussian profile plume mask employed for testing the various detectors. RMF of various loading levels were applied to this image from whose outputs the detection performance is evaluated and compared. There are two classes of performance evaluation metrics dominant in the literature, those derived from SCR and those from the receiver operation characteristic (ROC). In our work, we will use a related metric, area under curve (AUC). The reason will be explained in Sec. 4.3.

The steering vector and background covariance were estimated as follows. Figure 13 exhibits 10 steering vector candidates, $[\boldsymbol{s}_1, \ldots, \boldsymbol{s}_{10}]$, we used throughout the experiments. These signatures were computed by embedding the center pixel of the testing plume by different amounts of gas and dividing the radiance difference by the concentration pathlength (CL). The disagreement level in Euclidean and Mahalanobis degrees were computed with reference to the first signature $\boldsymbol{s}_1$. Strictly speaking, the "in-scene" signature is dependent on the individual pixel off-plume radiance, however, since the pixel radiance covered by the testing mask is quite homogeneous, we can expect the mismatch of signature to be dominated by the concentration difference. The estimation of the covariance matrix requires a separate embedding by the corruption masks given in Figs. 12(b), 14, and 15.

4.3 *Performance Evaluation Metric*

The ROC is the preferred metric for evaluating detectors, as it directly relates the probability of detection and false alarm

Downloaded From: http://opticalengineering.spiedigitallibrary.org/ on 03/28/2013 Terms of Use: http://spiedl.org/terms

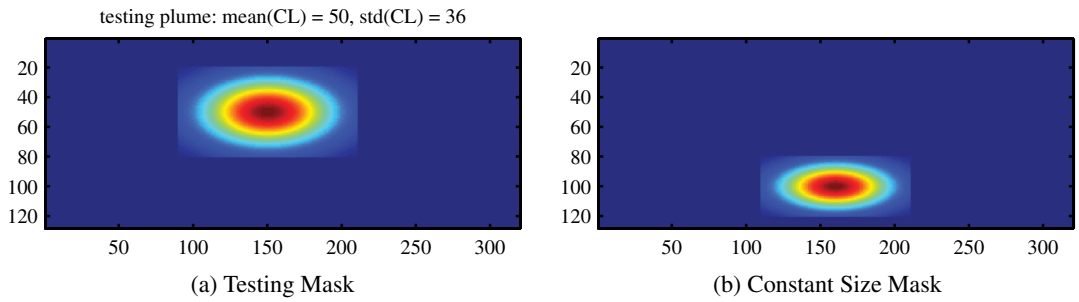

Fig. 12 (a) Mask employed to generate the plume used to test the proposed detectors and (b) a constant size plume mask used for computing contaminated covariance matrix.

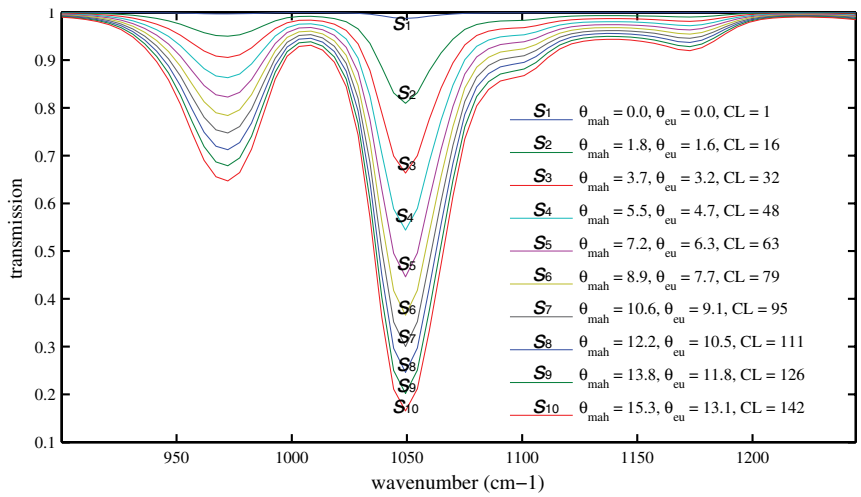

Fig. 13 Generated steering vector bank with different levels of mismatch.

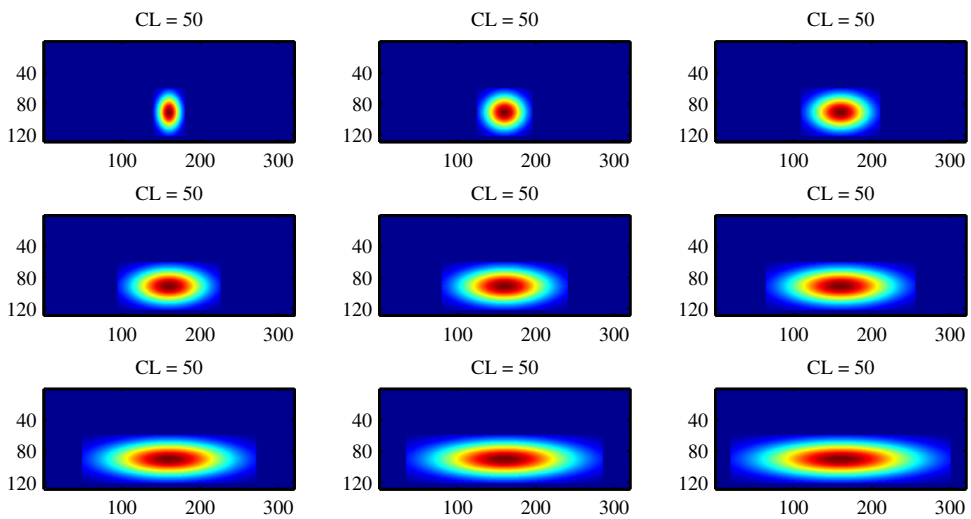

Fig. 14 Set of masks with increasing size, with average gas concentration at each pixel remaining constant.

rate. However, the SCR is acceptable, as long as it is consistent with the ROC, and can be easier to work with due to its mathematical tractability and availability of performance degradation expressions. Figure 16 compares the corresponding AUC scores and SCR scores shown in Fig. 9(a). From the plots, we can draw the conclusion that, although there is no one-to-one relationship between the two scores, in general, higher SCR values correspond to higher AUC values. Part of the difference in the shapes of the SCR and AUC plots is due to the AUC saturating at 1 while the SCR does not saturate. This conclusion validates our use of the SCR metric in Sec. 3.

While conducting diagonal loading experiments, we observed scenarios when higher SCR values do not guarantee better ROC curves. Such scenarios can be clearly illustrated by the pair of detector output score histograms due to

Downloaded From: http://opticalengineering.spiedigitallibrary.org/ on 03/28/2013 Terms of Use: http://spiedl.org/terms

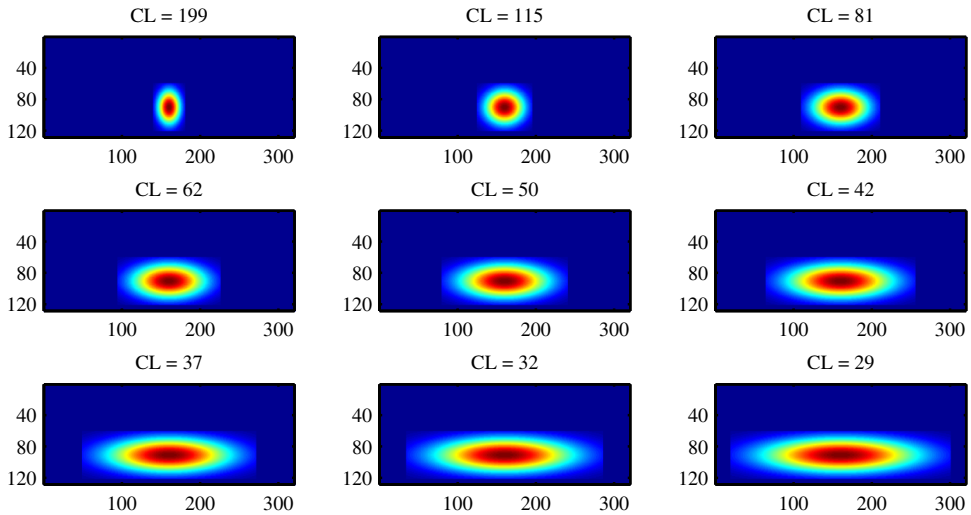

Fig. 15 Set of masks with increasing size, with the amount of gas within each the mask held constant.

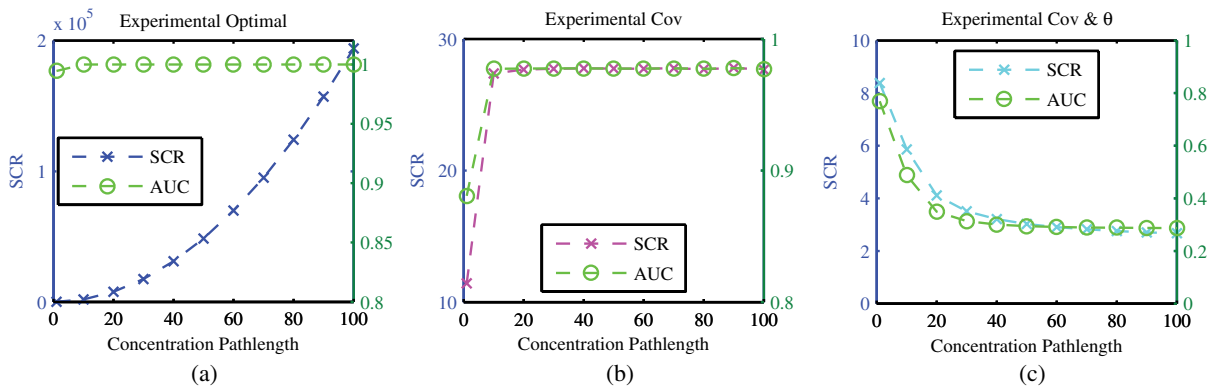

Fig. 16 AUC plots (green curves) for constant mask linear embedding in Fig. 9(a). Corresponding SCR plots are in the same color as in Fig. 9(a).

different diagonal loading levels in Fig. 17. The blue histogram corresponds to background pixel scores and the red histogram to plume pixels. AUC and SCR metrics are displayed for comparison. It can be clearly seen that Fig. 17(a) exhibits higher AUC and lower SCR than Fig. 17(b). The explanation for this phenomenon is that the absolute value of target score is not meaningful as long as it exceeds the predefined detector threshold in ROC based metrics. However, large target scores will contribute even more significantly to, or sometimes dominate SCR values because of the quadratic relationship as defined in Eq. (27). Therefore, we will use the AUC metric in this section.

4.4 *Performance Improvement*

In order to compensate for the various sources of performance loss, we investigate the performance improvement potential resulting from diagonal loading technique. In the

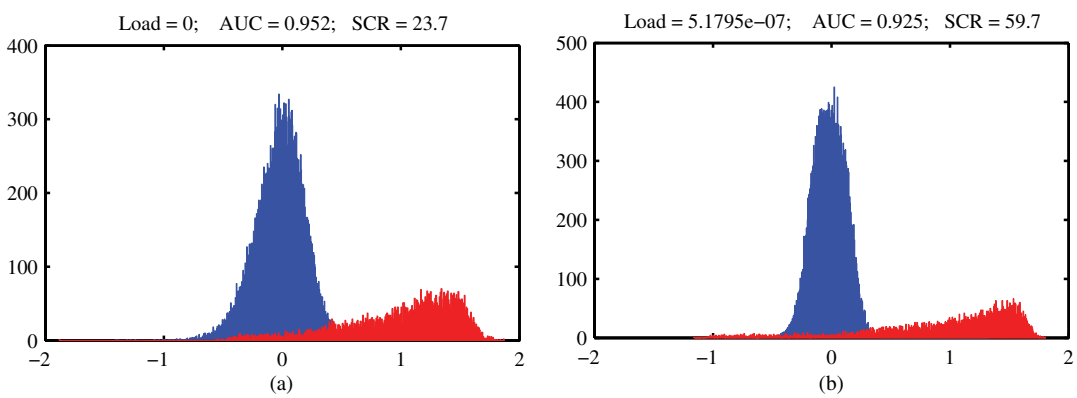

Fig. 17 Detector output score histograms of background pixels (blue) and plume pixels (red) with two diagonal loading levels (a) and (b).

Downloaded From: http://opticalengineering.spiedigitallibrary.org/ on 03/28/2013 Terms of Use: http://spiedl.org/terms

first set of experiments, a wide range of diagonal loading levels from 0 to 10^4 is examined to see how the detection performance varies. We choose steering vector $\boldsymbol{s}_1$ and a constant corruption mask [Fig. 12(b)] with CL = 50 ppm-m. The detector output image of each loading level is shown in Fig. 18. In the first row where the loading level is zero or very small, center pixels within the plume are missed by the detector because the supposed steering vector $\boldsymbol{s}_1$ is far away from the actual signature of the thick plume area. By inspecting the last row where loading factors are highest, the structure of the background is visible, which means the suppression on these pixels is not sufficient. The optimal loading level is on the order of 10^{-5}, and the corresponding ROC curves and AUCs due to different loading levels can be seen in Fig. 19. From Fig. 19(b), we can also find that a wide range of loading levels can improve the detection performance compared with the matched filter.

We now expand our previous experiment to four sets of experiments by embedding the image using the first steering vector $\boldsymbol{s}_1$ in Fig. 13 and selecting other steering vectors within the generated library, $[\boldsymbol{s}_2, \ldots, \boldsymbol{s}_{10}]$, with different degrees of mismatch and covariance of different contamination levels as parameters in the filter design. In each case, the optimal performance improvement is determined by selecting the proper diagonal loading level as a function of the different factors.

The first set of experiments involves investigation of the dependence of RMF robustness on the steering vector. We still choose the constant corruption mask and vary the steering vector index from 1 to 10. Figure 20(a) shows that RMF (blue line), is universally robust for appropriate selection of loading level [Fig. 20(b)] while matched filter performance (red line) degrades severely when steering vector index is greater than 7. The reason for such degradation is that most contaminated pixels within the Gaussian profile testing plume correspond to actual steering vector index 3 to 7. The curvature of loading levels is opposite to the one of matched filer performance (red line) because severe degradation requires heavier loading.

The second set of experiments illustrates loading effects for various degrees of covariance contamination. We choose the steering vector index number 1 and vary the average CL

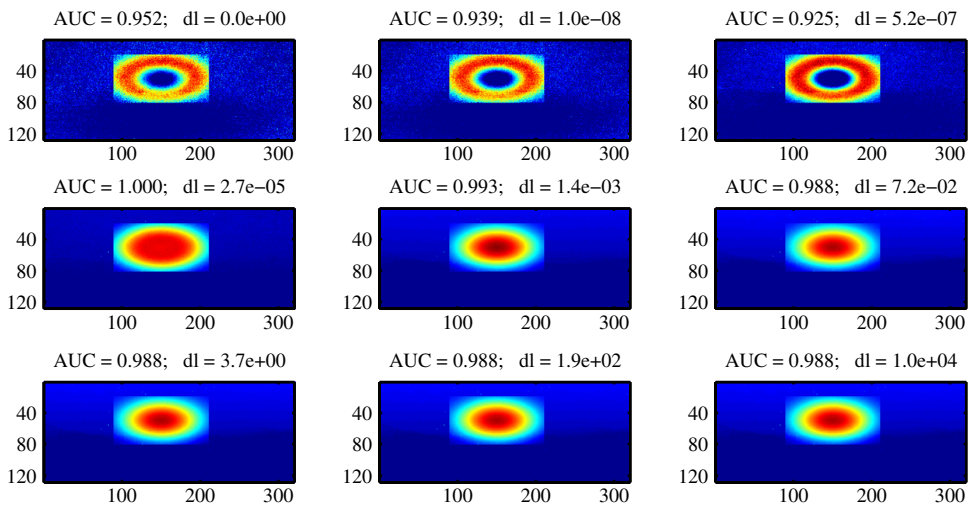

Fig. 18 Detector output image corresponding to a wide range of diagonal loading levels from 0 to 10^4.

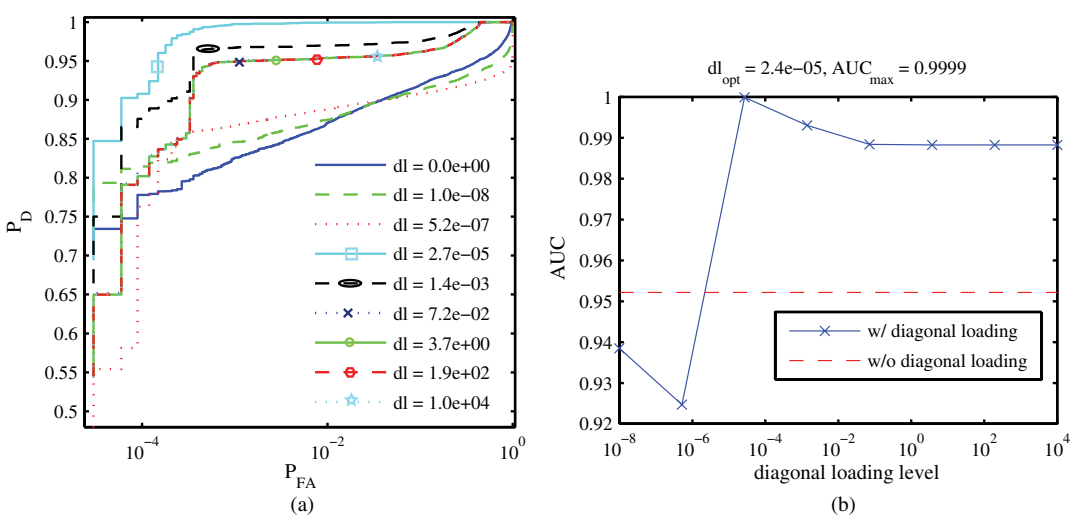

Fig. 19 (a) ROC curves with respect to different loading levelsand (b) AUCs corresponding to different loading levels.

Downloaded From: http://opticalengineering.spiedigitallibrary.org/ on 03/28/2013 Terms of Use: http://spiedl.org/terms

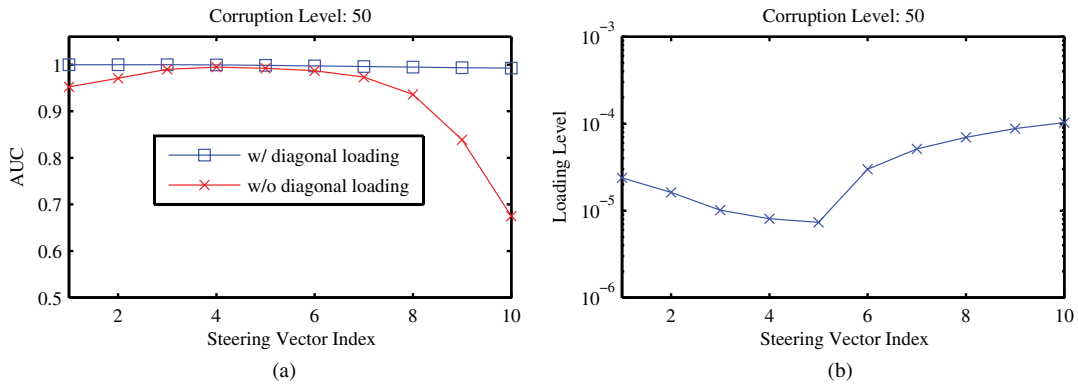

Fig. 20 (a) AUCs for different selections of steering vectors from index 1 to 10; (b) the appropriate diagonal loading levels resulting in optimal detection performance.

of the constant corruption mask from 10 to 100 ppm-m. As seen from Fig. 21(a), the performance of RMF remains superior despite heavier plume contamination. The performance drop of matched filter (red line) around CL = 20 ppm-m is because most pixels under the testing plume are of similar concentration, that is 20 ppm-m. The monotonic increase of the loading level in Fig. 21(b) is a direct result of increasing plume thickness; that is, the sample covariance is less trustworthy and the weight of identity matrix is consequently increasing.

The third and fourth sets of experiments probe the effects of fill factor by varying the corruption plume size, using the set of embedding masks from Figs. 14 and 15. The gas CL is held constant at 50 ppm-m in Fig. 14, so increasing the plume size results in a monotone increase in the covariance corruption. By contrast, Fig. 15 keeps the amount of gas unchanged during the increase of corruption mask size, so the average CL is monotonically decreasing. We choose steering vector index 5 and 10 in these two sets of experiments, respectively. Figure 22(a) illustrates that diagonal loading prevents the performance degradation, and when a majority of pixels are corrupted the diagonal loading term will dominate the sample covariance [Fig. 22(b)]. Figure 23(a) shows that the detection performance is well

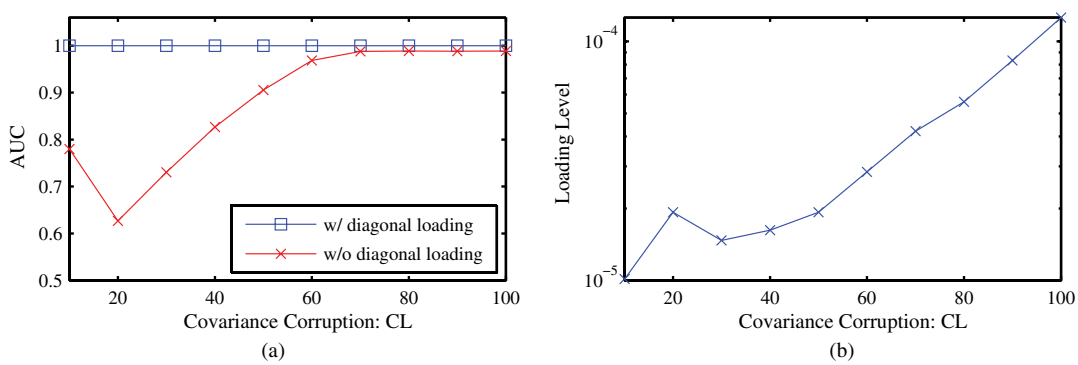

Fig. 21 (a) AUC improvements of diagonal loading with respect to different thickness of corruption plume and (b) corresponding optimal diagonal loading levels.

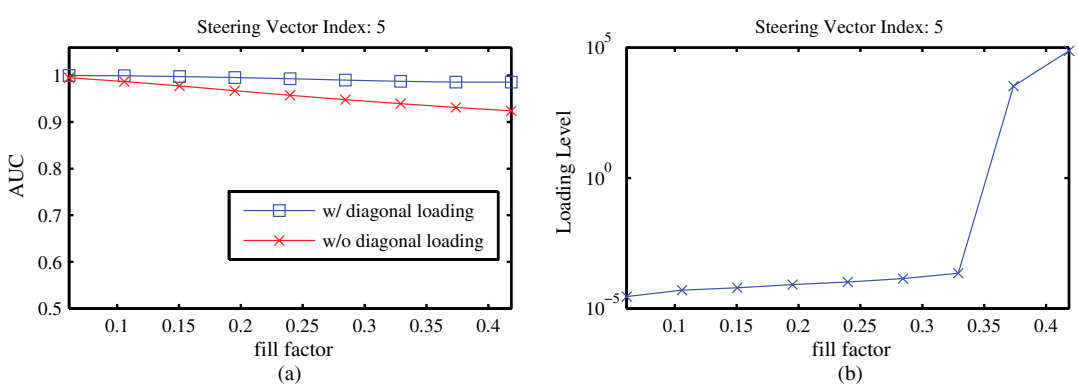

Fig. 22 (a) Performance improvements on AUC when the fill factor is increasing and average CL remains constant and (b) corresponding optimal loading levels.

Downloaded From: http://opticalengineering.spiedigitallibrary.org/ on 03/28/2013 Terms of Use: http://spiedl.org/terms

preserved by properly selecting loading level (blue line) while the matched filter performance (red line) decreases monotonically as the fill factor increases.

We have illustrated the potential detection performance improvement by diagonal loading. However, the question of choosing the correct loading factor remains to be addressed. A full analysis of this latter problem is out of the scope of this paper. However, we will now demonstrate a heuristic technique for choosing the loading factor that performs well empirically. These results suggest that diagonal loading may be used profitably even with approximate solutions to the loading factor optimization problem.

There are three major causes of detection degradation for which we need to compensate, including signature mismatch, contaminated gas strength, and contaminated gas fill factor. In Figs. 20–23, experiments have shown that the stronger (heavier) signature mismatch (covariance corruption) is, the larger a diagonal loading level is required. Although a theoretical relationship between the optimal loading level and uncertainties in both steering vector and estimated covariance is not available, we can still solve for a loading level that works well in practice from the nonlinear Eq. (36). The effectiveness of this method relies on our previous observation in Fig. 24(b), that a wide selection of diagonal loading levels can improve the detection performance greatly. In other words, our robust detector also exhibits its robustness in diagonal loading level β^{-1}.

In Fig. 24, we solve for the "optimal" diagonal loading levels according to the relationship of Eq. (36) for different degrees of steering vector disagreement. As in the other experiments, the true steering vector is chosen as the first one s_1 of our steering vector bank in Fig. 13, and other steering vectors within the bank are consecutively selected to incorporate larger uncertainty in steering vector. Instead of using the unobservable true covariance Σ_v, we feed Eq. (38) with a contaminated covariance Σ obtained in the first set of our experiments. The resulting loading levels are plotted in Fig. 24(b). As shown, the value range of β^{-1} is from 10^{-5} to 3×10^{-2}. If we choose a diagonal loading level artificially, say 5×10^{-4}, which is near to the median of the β^{-1} value range, the resulting detector can be applied to all the four experiments, with results shown in Fig. 25. The green line with asterisk marker represents the performance of this detector with $\beta^{-1} = 5 \times 10^{-4}$. Its improvement in detection performance is very close to the one from the optimal loading level indicated by the blue line square marker and can be a dramatic improvement over the matched filter performance represented by the red line cross marker. If a different β^{-1} is chosen, a similar result is shown in Fig. 26 for

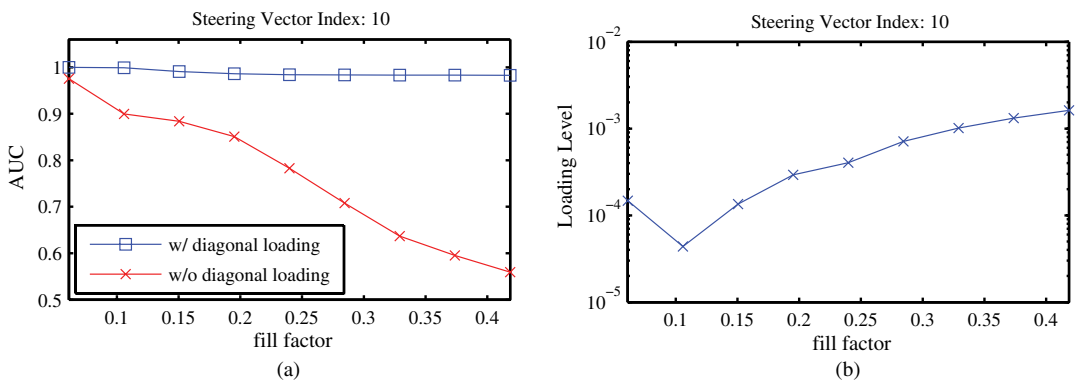

Fig. 23 (a) Performance improvements on AUC when the fill factor is increasing and total amount of gas remains constant and (b) corresponding optimal loading levels.

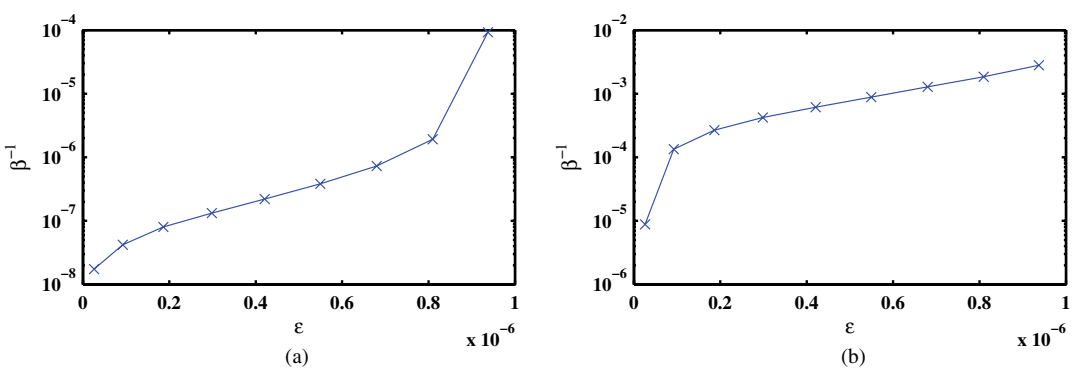

Fig. 24 Estimated diagonal loading levels from Eq. (36) for different amount of steering vector disagreement introduced in Fig. 13 using (a) uncontaminated covariance Σ_v (for comparison purpose only) and (b) signal contaminated covariance Σ (which is used in subsequent experiments).

Downloaded From: http://opticalengineering.spiedigitallibrary.org/ on 03/28/2013 Terms of Use: http://spiedl.org/terms

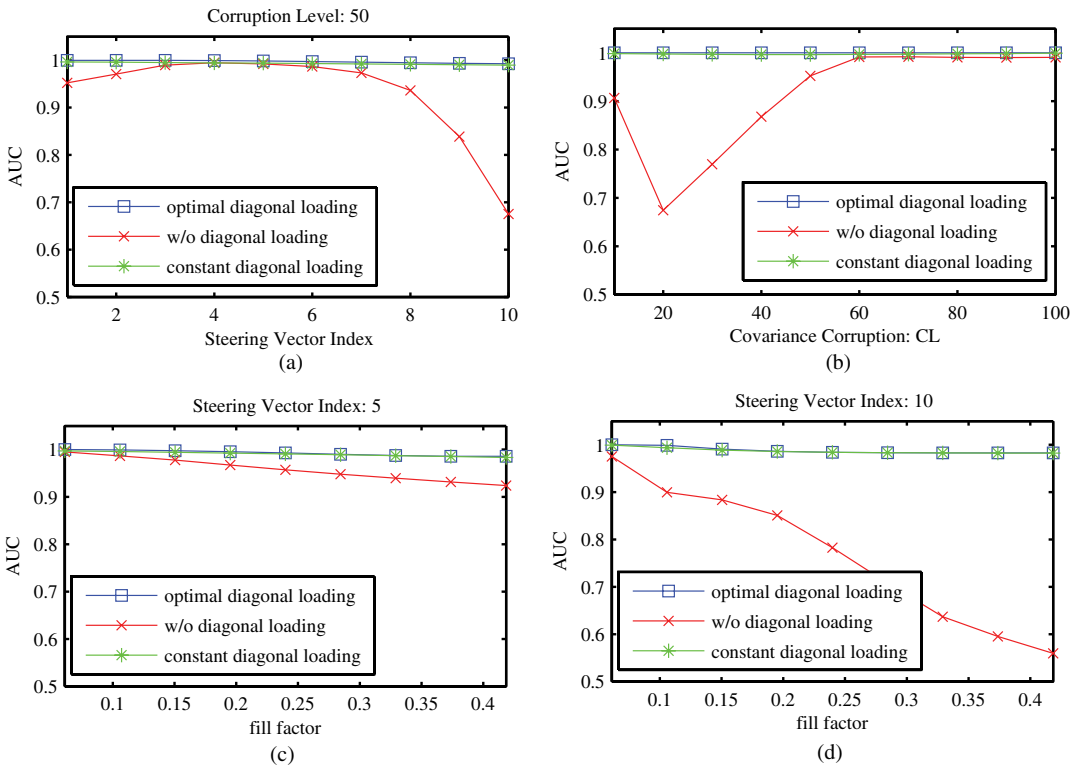

Fig. 25 Performance comparison when a constant diagonal loading level is $\beta^{-1} = 5 \times 10^{-4}$ is used for all four experiments: (a) experiment I; (b) experiment II; (c) experiment III; and (d) experiment IV.

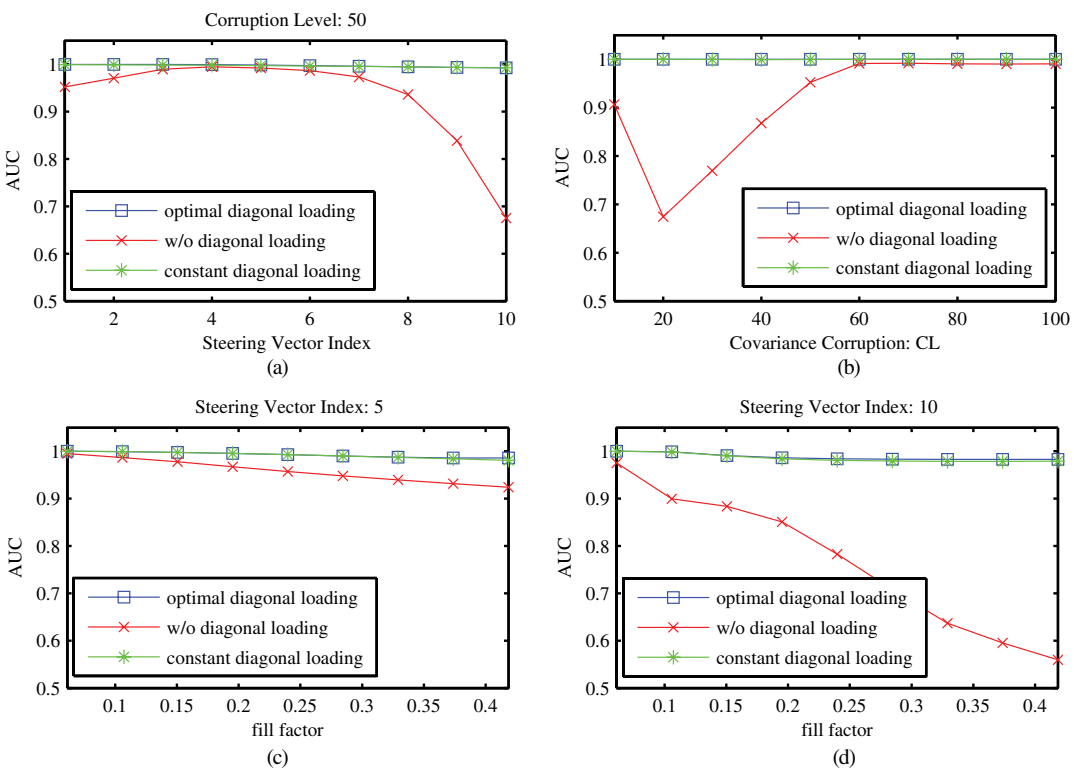

Fig. 26 Performance comparison when a constant diagonal loading level is $\beta^{-1} = 1 \times 10^{-4}$ is used for all four experiments: (a) experiment I; (b) experiment II; (c) experiment III; and (d) experiment IV.

Downloaded From: http://opticalengineering.spiedigitallibrary.org/ on 03/28/2013 Terms of Use: http://spiedl.org/terms

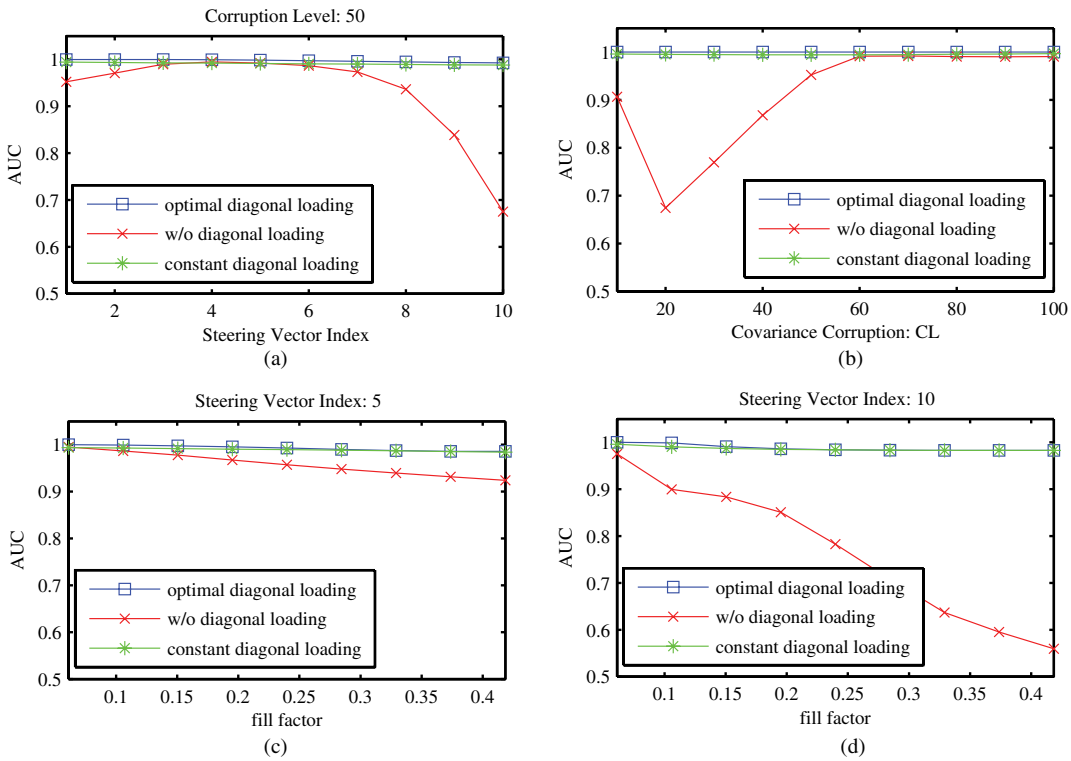

Fig. 27 Performance comparison when a constant diagonal loading level is $\beta^{-1} = 1 \times 10^{-3}$ is used for all four experiments: (a) experiment I; (b) experiment II; (c) experiment III; and (d) experiment IV.

$\beta^{-1} = 1 \times 10^{-4}$ and in Fig. 27 for $\beta^{-1} = 1 \times 10^{-3}$. As a consequence of this observation, it is not necessary to solve for the exact value of the optimal loading factor. An empirical loading factor would be enough to improve the detection performance to a similar level and can be easily calculated by numerically solving a nonlinear Eq. (36), given that an estimate of uncertainty in steering vector ϵ is available.

5 Conclusions

Vapor phase chemical hyperspectral detection algorithms can be severely degraded by a mismatch between the observed chemical spectral signatures and those from a library, and contamination of estimates of the background statistics by the gaseous plume. Both of these effects occur routinely in practice. In this paper, a radiative transfer model was used to simulate the presence of a chemical plume over a measured background scene. The performance loss of the AMF due to various factors was studied, including steering vector mismatch, covariance matrix contamination, and plume-background correlation, both individually and in combination. In order to mitigate this degradation, a robust matched filter employing diagonal loading was applied. The resulting detection improvements show that a wide range of diagonal loading levels can be effective in reversing the performance losses due to the factors considered.

Acknowledgments

This work is sponsored by Defense Threat Reduction Agency (DTRA) Joint Science and Technology Office—Chemical and Biological Defense (JSTO-CBD) program, under Air Force Contract FA8721-05-C-0002. Opinions, interpretations, conclusions, and recommendations are those of the authors and not necessarily endorsed by the United States Government.

References

1. D. Manolakis, G. Shaw, and N. Keshava, "Comparative analysis of hyperspectral adaptive matched filter detector," *Proc. SPIE* **4049**, 2–17 (2000).
2. S. J. Young, "Detection and quantification of gases in industrial-stack plumes using thermal-infrared hyperspectral imaging," Tech. Rep. ATR-2002(8407)-1, The Aerospace Corporation, pp. 21–27 (2002).
3. D. W. Messinger, "Gaseous plume detection in hyperspectral images: a comparison of methods," *Proc. SPIE* **5425**, 592–603 (2004).
4. B. Foy, J. Theiler, and A. Fraser, "Unreasonable effectiveness of the adaptive matched filter," in *Proc. MSS (Military Sensing Symposia) Passive Sensors Conference* (2006).
5. K. Gerlach, "The effects of signal contamination on two adaptive detectors," *IEEE Trans. Aero. Electron. Syst.* **31**(1), 297–309 (1995).
6. S. Matteoli, M. Diani, and G. Corsini, "Improved estimation of local background covariance matrix for anomaly detection in hyperspectral images," *Opt. Eng.* **49**(4), 046201 (2010).
7. C. Khatri and C. Rao, "Effects of estimated noise covariance matrix in optimal signal detection," *IEEE Trans. Acoust. Speech Signal Process.* **35**(5), 671–679 (1987).
8. H. Cox, "Resolving power and sensitivity to mismatch of optimum array processors," *J. Acoust. Soc. Am.* **54**(3), 771–785 (1973).
9. I. S. Reed and X. Yu, "Adaptive multiple-band CFAR detection of an optical pattern with unknown spectral distribution," *IEEE Trans. Acoust. Speech Signal Process.* **38**(10), 1760–1770 (1990).
10. J. Theiler and B. Foy, "Effect of signal contamination in matched-filter detection of the signal on a cluttered background," *Geosci. Remote Sens. Lett.* **3**(1), 98–102 (2006).
11. J. Theiler, B. R. Foy, and A. M. Fraser, "Nonlinear signal contamination effects for gaseous plume detection in hyperspectral imagery," *Proc. SPIE* **6233**, 62331U (2006).
12. H. Cox, R. Zesking, and M. Owen, "Robust adaptive beamforming," *IEEE Trans. Acoust. Speech Signal Process.* **35**(10), 1365–1376 (1987).
13. J. Ward, H. Cox, and S. M. Kogon, "A comparison of robust adaptive beamforming algorithms," in *Conf. Record of the 37th Asilomar Conf. on Signals, Systems and Computers*, Vol. 2, pp. 1340–1344, IEEE (2003).

Downloaded From: http://opticalengineering.spiedigitallibrary.org/ on 03/28/2013 Terms of Use: http://spiedl.org/terms

14. O. Besson and F. Vincent, "Performance analysis of beamformers using generalized loading of the covariance matrix in the presence of random steering vector errors," *IEEE Trans. Signal Process.* **53**(2), 452–459 (2005).
15. J. Li, P. Stoica, and Z. Wang, "On robust capon beamforming and diagonal loading," *IEEE Trans. Signal Process.* **51**(7), 1702–1715 (2003).
16. D. F. Flanigan, "Prediction of the limits of detection of hazardous vapors by passive infrared with the use of modtran," *Appl. Opt.* **35**(30), 6090–6098 (1996).
17. V. Farley et al., "Performance of the FIRST, a longwave infrared hyperspectral imaging sensor," *Proc. SPIE* **6398**, 63980T (2006).
18. S. W. Sharpe et al., "Gas-phase databases for quantitative infrared spectroscopy," *Appl. Spectrosc.* **58**(12), 1452–1461 (2004).

Sidi Niu is currently a PhD candidate and research assistant in the Department of Electrical and Computer Engineering at Northeastern University. His research interests include hyperspectral image processing, remote sensing, digital image processing, pattern recognition, and computer vision. He received his MS from Northeastern University and BS from Zhejiang University, China, both in electrical engineering.

Steven E. Golowich is a technical staff member at MIT Lincoln Laboratory, where his research interests include statistical signal processing, hyperspectral imaging, synthetic aperture radar, and structured light. He was awarded a PhD in physics by Harvard University and an AB in physics and mathematics by Cornell University. Previously, he was a member of technical staff at the Bell Labs Mathematical Sciences Research Center and taught at Princeton University. He is a recipient of the American Statistical Association Outstanding Application award and the Wilcoxon Prize.

Vinay K. Ingle is currently an associate professor in the Department of Electrical and Computer Engineering at Northeastern University, where he has been since 1981 after receiving his PhD in electrical and computer engineering from Rensselaer Polytechnic Institute. He has taught both undergraduate and graduate courses in many diverse areas including systems, signal/image processing, communications, and control theory. He has co-authored several textbooks on signal processing including digital signal processing using MATLAB (Cengage, 2012, 3rd ed.), applied digital signal processing (Cambridge University Press, 2011), and statistical and adaptive signal processing (Artech House, 2005). He has broad research experience in the areas of signal and image processing, stochastic processes, and estimation theory. Currently he is actively involved in hyperspectral imaging and signal processing.

Dimitris G. Manolakis received his education (BS in physics and PhD in electrical engineering) from the University of Athens, Greece. He is currently a senior member of the technical staff at MIT Lincoln Laboratory, in Lexington, Massachusetts. Previously, he was a principal member, research staff, at Riverside Research Institute. He has taught at the University of Athens, Northeastern University, Boston College, and Worcester Polytechnic Institute; and he is coauthor of the textbooks Digital Signal Processing: Principles, Algorithms, and Applications (Prentice-Hall, 2006, 4th ed.), Statistical and Adaptive Signal Processing (Artech House, 2005), and Applied Digital Signal Processing (Cambridge University Press, 2011). His research experience and interests include the areas of digital signal processing, adaptive filtering, array processing, pattern recognition, remote sensing, and radar systems.

Downloaded From: http://opticalengineering.spiedigitallibrary.org/ on 03/28/2013 Terms of Use: http://spiedl.org/terms